

# Multi-wavelength study of X-ray luminous clusters at $z \sim 0.3$

## I. Star formation activity of cluster galaxies

F. G. Braglia<sup>1,3</sup>, D. Pierini<sup>1</sup>, A. Biviano<sup>2</sup>, and H. Böhringer<sup>1</sup>

<sup>1</sup> Max-Planck-Institut für extraterrestrische Physik, Giessenbachstrasse 1, D-85748 Garching bei München, Germany  
e-mail: fbraglia@mpe.mpg.de; dpierini@mpe.mpg.de; hxb@mpe.mpg.de

<sup>2</sup> INAF-Osservatorio Astronomico di Trieste, via G. B. Tiepolo 11, I-34143 Trieste, Italy  
e-mail: biviano@oats.inaf.it

<sup>3</sup> University of British Columbia, Dept. of Physics and Astronomy, 6224 Agricultural Road, V6T 1Z1 Vancouver BC, Canada  
e-mail: fbraglia@phas.ubc.ca

### ABSTRACT

**Context.** The current paradigm of cosmic formation and evolution of galaxy clusters foresees growth mostly through merging. Galaxies in the infall region or in the core of a cluster undergo transformations owing to different environmental stresses.

**Aims.** For two X-ray luminous clusters at redshift  $z \sim 0.3$  with opposite X-ray morphologies (i.e., dynamical states), RXCJ 0014.3-3022 and RXCJ 2308.3-0211, we assess differences in galaxy populations as a function of cluster topography. This is a pilot study for the joint X-ray and optical analysis of the REFLEX-DXL cluster sample.

**Methods.** Cluster large-scale structure and substructure are determined from the combined photometry in the B, V, and R bands, and from multi-object optical spectroscopy at low resolution. Photometric redshifts and broad-band optical colours are determined. A spectral index analysis is performed, based on the [O II]( $\lambda\lambda 3726, 3728 \text{ \AA}$ ) and H $\delta$ ( $\lambda 4102 \text{ \AA}$ ) features, and the D4000 break, which are available for more than 100 member galaxies per cluster. Additional far-ultraviolet (FUV) photometry is retrieved from the GALEX archive. Combination of spectral indices and FUV-optical colours provides a picture of the star formation history in galaxies.

**Results.** In spite of the potential presence of a small fraction of galaxies with obscured star formation activity, the average star-formation history of cluster members is found to depend on cluster-centric distance and, more interestingly, on substructure. The core regions of both clusters mainly host galaxies dominated by old, passively evolving stellar populations, which define the same red sequence in a  $(B - R)$  colour- $R$  magnitude diagram. However, there is a sharp increase in star formation activity along two well-defined filamentary structures of the merging cluster RXCJ 0014.3-3022, out to its virial radius and beyond. It is produced by luminous (i.e., with  $L_R \geq L_R^*$ ) and sub- $L^*$  galaxies. Conversely, the regular cool-core cluster RXCJ 2308.3-0211 mostly hosts galaxies which either populate the red sequence or are becoming passive. This holds out to its virial radius, and also for its large-scale environment.

**Conclusions.** These results suggest the existence of a correspondence between assembly state and overall age of the stellar populations of galaxies inside the virialized region and in the surrounding large scale structure of massive clusters at  $z \sim 0.3$ .

**Key words.** galaxies: clusters: individual: Abell 2744, AC 118, Abell 2537 – galaxies: evolution – galaxies: stellar content – cosmology: observations – X-rays: galaxies: clusters

## 1. Introduction

X-ray emitting clusters signpost the largest amounts and concentrations of (cold) dark matter (CDM) in bound systems. At the same time, they provide large samples of coeval galaxies within a well-defined environment. This enables to study how galaxy properties, like star formation rate (SFR), behave as a function of environment and local density.

Detailed numerical simulations confirm that clusters tend to form at the intersection of filaments and sheets in the evolving large-scale structure of the Universe: over time, matter falls along such structures and accretes into a cluster. The infall pattern is not random: paths show a correlation in time and are almost stable, so that matter is channelled into a cluster through filamentary structures with persistent geometry. Matter does not accrete in a steady and continuous way, but in clumps and bound structures, which can be identified as infalling groups of galaxies or less massive clusters (Colberg et al. 1999).

The existence of extended filamentary structures and voids in the large-scale spatial distribution of local galaxies is known since the advent of redshift surveys (e.g. Gregory and Thompson 1978; Davis et al. 1982). Deep X-ray imaging of the emission from hot ( $10^5$ – $10^7$  K) gas and analysis of the two-dimensional distribution of galaxies at the same (photometric or spectroscopic) redshift of a cluster have extended the detection of filamentary networks around clusters up to redshift  $z \sim 0.6$  (e.g. Kull & Böhringer 1999; Scharf et al. 2000; Kodama et al. 2001; Zappacosta et al. 2002; Durret et al. 2003; Ebeling et al. 2004; Dietrich et al. 2005).

The galaxy populations in cluster-feeding filaments can be expected to differ somewhat from those in the cluster main body or in the adjacent field, as filaments are an environment of transition between the low and extremely high density regimes. Consistently, observations have revealed a clear correlation between galaxy morphology or SFR and local density or cluster-centric distance (Dressler et al. 1980; Dressler et al. 1997; Whitmore et al. 1993; Balogh et al. 1997). The past and present star-formation activities of galaxies appear to be different in low

and high density environments already at intermediate redshifts (Abraham et al. 1996; Morris et al. 1998; Poggianti et al. 2006). From a spectral index analysis of galaxies in 15 X-ray luminous clusters at  $0.18 < z < 0.55$ , Balogh et al. (1999) concluded that the increase in the observed star-formation activity towards the outer regions of clusters is consistent with an age sequence: galaxies in cluster outskirts have experienced star-formation phases more recently than galaxies in cluster cores. Their interpretation was that the truncation of star formation in cluster galaxies may largely be a gradual process, perhaps due to the exhaustion of gas in galaxy discs over fairly long timescales. In this case, differential evolution may result because field galaxies can refuel their discs with gas from extended halos, thus regenerating star formation, while cluster galaxies may have lost such gaseous halos as well as the dark matter ones (cf. Halkola et al. 2007), and so continue to evolve passively.

Combining X-ray and optical observations, Böhringer et al. (2006) and Braglia et al. (2007, hereafter referred to as BPB07) provided evidence for the presence of two filaments out from the main body of the cluster RXCJ 0014.3–3022 (alias Abell 2744, AC 118) and extending beyond its virial radius. This is one of the 13 clusters at  $z = 0.27–0.31$  with X-ray luminosity higher than  $10^{45} \text{ erg s}^{-1} \text{ cm}^{-2}$ , selected from the ROSAT-ESO Flux Limited X-ray (REFLEX) cluster survey (Böhringer et al. 2001a) and observed with XMM-Newton, which make the Distant X-ray Luminous (DXL) cluster sample (Zhang et al. 2006). It is also a major-merger system (e.g. Boschin et al. 2006) and a “Butcher-Oemler” cluster (Butcher & Oemler 1978a, 1978b, 1984). The blue galaxies in the cluster core, that are more abundant compared to present-day massive clusters, are mostly systems involved in major mergers but sub- $L^*$  even in this brightened phase; in their faded state they appear destined to become dwarfs (Couch et al. 1998). In addition, BPB07 found evidence for luminous galaxies along the two filaments which exhibit a boosted star-formation activity with respect to their counterparts in the field.

More recent studies seem to confirm the increase of star formation activity along filaments in the outskirts of clusters. For instance, Fadda et al. (2008) report the presence of twice as many dusty starbursts along two filamentary structures connecting the clusters Abell 1770 and Abell 1763 ( $z = 0.23$ ) as in other cluster regions. Furthermore, Porter et al. (2008) find a significant enhancement of star formation, mostly in dwarf galaxies ( $M_B > -20$ ), from a sample of 52 supercluster-scale filaments of galaxies joining pairs of rich clusters of galaxies within the 2-degree Field Redshift Survey region. This work consolidates a similar result obtained for the Pisces-Cetus Supercluster filaments (Porter & Raychaudhury 2007).

The presence of dwarf and giant galaxies with enhanced SFR and the wealth of available data make the merging cluster RXCJ 0014.3–3022 an interesting laboratory to study how different physical processes affect galaxy evolution in different cluster environments. To better understand the importance of substructure on star-formation activity in cluster galaxies, we investigate the DXL cluster RXCJ 2308.3–0211 (alias Abell 2537), a cool core (thus relaxed) system, in addition to RXCJ 0014.3–3022. The analysis presented here shows the power of combining X-ray observations, wide-field optical imaging, and multi-object spectroscopy for such a study (see also Böhringer et al. 2001b, 2006, 2007; BPB07; Pierini et al. 2008). Results from a similar analysis applied to the entire REFLEX-DXL sample will be presented in future papers of this series.

This first paper presents in detail data reduction and analysis techniques, in addition to the results obtained for RXCJ 0014.3–

3022 ( $z=0.3068$ ) and RXCJ 2308.3–0211 ( $z=0.2966$ ). It is organised as follows. Section 2 provides information on data quality and reduction, whereas Sect. 3 describes the construction of the photometric and spectroscopic catalogues, and the results obtained from an analysis of the two cluster morphologies and a spectral index analysis for a representative sample of cluster galaxies. A comprehensive discussion follows (Sect. 4), whereas conclusions are summarised in Sect. 5.

Hereafter we adopt a  $\Lambda$ CDM cosmology where  $\Omega_m = 0.3$ ,  $\Omega_\Lambda = 0.7$ , and  $h_{70} = H_0/70 \text{ km s}^{-1} \text{ Mpc}^{-1} = 1$ . At the average cluster redshift, 1 arcmin corresponds to 0.267 Mpc.

## 2. Data: description and reduction

### 2.1. X-ray imaging

RXCJ 0014–3022 and RXCJ 2308.3–0211 were observed with XMM-Newton in AO-1 and AO-3 as part of the REFLEX-DXL cluster sample (Zhang et al. 2006). Total exposure times were equal to 18.3 and 12 ks, respectively. Observations were performed with thin filter for the three EPIC detectors: MOS data were collected in Full Frame (FF) mode, while *pn* data were taken in Extended Full Frame (EFF) in AO-1 and FF mode in AO-3, respectively. For *pn*, the fractions of the out-of-time (OOT) effect are 2.32% and 6.30% for the EFF mode and FF mode, respectively. An OOT event file is created and used to statistically remove the OOT effect. We refer the reader to Zhang et al. (2006) for the entire description of data reduction. Here it is important to say that RXCJ 0014–3022 and RXCJ 2308.3–0211 have bolometric luminosities equal to  $2.12(\pm 0.17) \times 10^{45} \text{ erg s}^{-1}$  and  $1.20(\pm 0.13) \times 10^{45} \text{ erg s}^{-1}$ , respectively. Furthermore, they were classified as offset centre and single objects, respectively, according to the classification of the dynamical state based on X-ray imaging (Jones & Forman 1992). This corresponds to the different nature of the two clusters, one being a merging systems, the other a regular, centrally peaked, cool-core cluster (Zhang et al. 2006 and references therein).

### 2.2. Multi-object spectroscopy

Spectroscopic observations in regions of the sky encompassing RXCJ 0014.3–3022 and RXCJ 2308.3–0211 were performed on August 14 through 16, 2004 (4.4 hr per cluster) as part of the ESO Large Program 169.A–0595 (PI: H. Böhringer), carried out in ESO GO time in visitor and service modes. This program aims at maximising the number of member galaxies lying in a wide region centred at the X-ray centroid of a cluster, for 7 of the 13 DXL clusters. This is achieved through multi-object spectroscopy (MOS) in low resolution mode with VIMOS (VIsible Multi-Object Spectrograph), which is mounted at the Nasmyth focus B of VLT-UT3 *Melipal* at Paranal Observatory (ESO), Chile. VIMOS is a wide-field imager and multi-object spectrograph operating in the visible (from 3600 to 10,000 Å). It is made of four identical arms, each with a field of view (FOV) of  $7' \times 8'$  and a  $0.205''$  pixel size, separated by a gap between each quadrant of  $\sim 2'$ . Thus the total FOV is  $4 \times 7' \times 8'$ . Each arm is equipped with 6 grisms, providing a spectral resolution ranging from 200 (low) to 2500 (high), and one EEV CCD  $4k \times 2k$ .

Selection of targets for spectroscopy followed a strict luminosity criterion, in order to minimise the probability of bias on future results about cluster dynamics, galaxy populations, and star-formation activity, which can potentially be introduced by additional colour selection. I-band was chosen for pre-imaging, since it provides the closest analog to a selection in stellar mass

among the optical bands available for VIMOS. In fact, I-band probes emission from stellar populations mostly older than 1–2 Gyrs at  $z \sim 0.3$ , which are least affected by recent episodes of star-formation activity. As a consequence, different environments are sampled with equal probability, given the well-known existence of a correlation between density and star-formation activity (Dressler 1980; Whitmore et al. 1993).

Preimaging was executed adopting three different pointings with two ditherings of  $15''$  each, in order to allow the most complete coverage of the cluster central region, a good coverage of the cluster outskirts and sufficient overlap for the cross-shaped gaps between the CCDs. The three pointings are aligned in the E-W direction and partly overlapping, providing a total continuous coverage of about  $34'$  in R.A. and  $20'$  in DEC. This corresponds to an uninterrupted coverage of the cluster out to  $2.7h_{70}^{-1}$  Mpc and a fairly good coverage of the outskirts out to  $4.6h_{70}^{-1}$  Mpc at the clusters redshift (see Fig. 1).

An 8-min exposure time per pointing, coupled to the photon collecting area of the 8-m class VLT, enabled to completely sample galaxies down to  $I \sim 22.5$ , which corresponds to about  $M_I^* + 2$  for the RXCJ 0014.3-3022 core (see Couch et al. 1998), where  $M_I^*$  is the absolute magnitude corresponding to the characteristic luminosity ( $L^*$ ) of the I-band galaxy luminosity function (LF, see Schechter 1976). Detection and identification of galaxies, together with extraction of photometry, were accomplished through *SExtractor* (Bertin & Arnouts 1996). Galaxies with  $17 \leq I \leq 19$  or  $19 < I \leq 21.5$  were successively classified as bright or faint, respectively. Two VIMOS masks per pointing were prepared using the VMMPs tool from ESO<sup>1</sup>, one for the bright objects and one for the faint ones. The former were flagged as compulsory targets, whereas the latter were selected as targets by the software, with the only requirement that the number of objects per mask was maximised. This approach allowed spectra to be obtained for most of the bright galaxies without biasing the overall target selection; at the same time, the LF of cluster galaxies was sampled across  $L^*$ .

As for MOS observations, a minimum value of the signal-to-noise ratio (S/N) equal to 10 (5) was required for bright (faint) galaxies, which set the total exposure time equal to 6 (82) minutes. This time was broken in three exposures per mask, a total of six masks (three for bright objects and three for faint ones) covering the region containing each cluster. Mask were designed for the LR-Blue grism, which provides a spectral coverage from 3700 to 6700 Å (observed frame) at a spectral resolution of about 200 for a  $1''$  slitwidth, and does not suffer from fringing. For objects at  $z = 0.3$ , the wavelength range 2830–5130 Å was mapped, where important spectral features fall and were expected to be detected on the basis of the S/N requirements. Among them, the most relevant are the [OII], [OIII],  $H_\beta$ ,  $H_\gamma$ , and  $H_\delta$  emission lines, the CaII<sub>H+K</sub> absorption lines, and the 4000 Å break. These spectral features are extremely valuable to determine spectroscopic redshifts up to  $z \sim 0.8$  and increase their accuracy beyond that provided by the set-up. Thanks to the multiplexing capability of the LR-Blue grism, which enables to stack up to 4 spectra along the spectral dispersion direction, up to 150–200 spectra per mask were collected, depending on brightness and position of the targets. Designed slits across individual targets included a region of empty sky of  $3''$  length, to provide a suitable sky subtraction.

Data from the MOS observations previously described were reduced mainly using the dedicated software VIPGI<sup>2</sup>, which is a complete data reduction environment specifically developed to handle and reduce data from imaging, MOS and integral-field-unit spectroscopy with VIMOS. Its capabilities and quality have been tested against the reduction of many tens of thousands spectra from the VVDS, and are thoroughly explained in the aforementioned publications. In addition to bias and flat-field correction, multiplex spectra identification, sky subtraction, spectral reduction, and wavelength calibration, VIPGI is capable of data editing and redshift evaluation based on single- and multiple-line fitting, after manual selection of candidate lines to be matched with available line catalogues. Data reduction followed the standard approach, fully described in the VIPGI manual and in Scodreggio et al. (2005). A master bias frame was obtained, where possible, by combining all the available bias frames from the night; rejection of overscan areas and/or bad pixels was performed by standard  $3\sigma$  clipping through the data cube defined by the bias frames. In particular, the adjustment of initial guesses for wavelength calibration was usually fairly quick: a check of the line catalogue of the arcs always produced a good agreement with the positions of features in the arc spectra, so only small shifts of 1 to 3 pixels (i.e., about 4 to 15 Å at the resolution of the LR-Blue grism) were introduced as a correction. None of the quadrants was found to be tilted or rotated. The complete adjustment of the calibration arcs was usually performed with a small shift of less than 5 pixels (i.e., about 20 Å) on the dispersion direction. Spectra detection, based on the adjusted arc calibration, was performed using standard parameters too. After manual correction of shifted lines slit by slit, the wavelength calibration shows a typical rms of  $\sim 1.5$  Å.

As for science spectra, a combined reduction of the three frames per mask was performed with the *Reduce Sequence of Observations* tool of VIPGI. This avoids confusion with noise and residuals from non optimal bias removal and flat-field correction; in addition, it enables detection of objects that are fainter than expected. The minimum detection level was set equal to  $3\sigma$  for bright and faint targets, where sky subtraction was based on a fit with a 3rd-order polynomial over each single frame instead of using a simple median over the stack of three frames. This procedure was found to provide a better estimation of the sky emission and more robust detections: using a median-based sky subtraction instead, up to 15% of the faint targets could remain undetected. Spectra of individual targets were extracted using Horne's algorithm (Horne 1986); standard parameters for detection and deblending (i.e., disentangling of multiple spectra falling in the same slit) were used, as they provided a robust extraction. At the end, all spectra were inspected by eye to check if residual sky contamination, hot pixels, ghosts arising from the superposition of different spectral orders, and other artifacts were present, and if all targets had been successfully extracted. In addition, initial values of the S/N were computed for the continuum emission and spectral features.

Spectroscopic redshifts were mainly determined through VIPGI (the EZ<sup>3</sup> package, plus software for the manual detection and fit of spectral features). After a pipeline determination for all spectra, individual redshifts were inspected by eye and manual determination was executed in case of a probable misidentify-

<sup>1</sup> <http://www.eso.org/observing/p2pp/OSS/VMMPs>

<sup>2</sup> VIPGI (VIMOS Interactive Pipeline and Graphical Interface, Scodreggio et al. 2005) is developed by the VIRMOS Consortium to handle the reduction of the VIMOS data for the VVDS (VIMOS VLT Deep Survey, Le Fèvre et al. 2005)

<sup>3</sup> <http://cosmos.iasf-milano.inaf.it/pandora/>

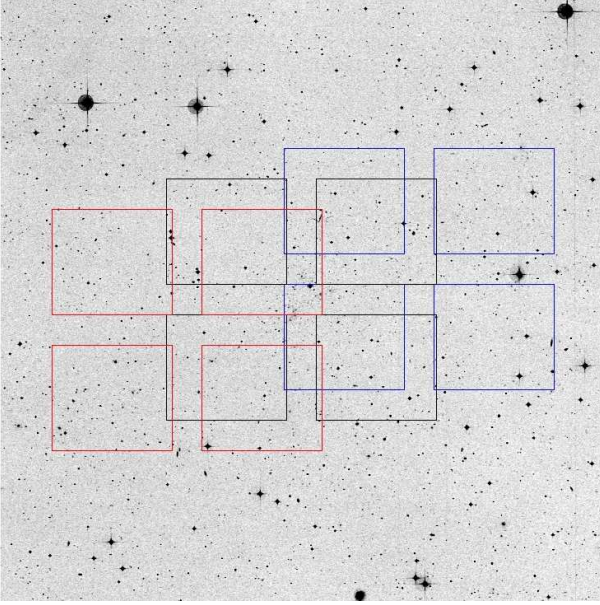


**Fig. 1.** Mask setup for the VIMOS observations of RXCJ 0014.3-3022, overlaid onto the corresponding DSS field. Each set of four boxes with the same colour represents one pointing; the VIMOS quadrants are aligned in the EW direction.

ing. In general, spectra with initial values of the S/N equal to 4 (at least) for the continuum and larger than 10 for spectral features enabled a clear determination of spectral types, and, thus, provided an unambiguous determination of redshifts. Typically a reliable spectrum could not be extracted from data with a mean S/N less than 3; the corresponding slits were flagged for removal. Non-detections were used to evaluate the mean spectral noise, which amounts to  $\sim 20$  counts/pixel, the blue spectral region covered by the LR-Blue grism (i.e.,  $\lambda < 5000$  Å) being slightly noisier than the red one. The faintest, reliably detected spectra have continuum fluxes from 100 to 500 counts/pixel, depending on the spectral type, and spectral features with high S/N.

### 2.3. Wide-field imaging

Optical photometry was carried out using the wide-field imager (WFI) mounted at the Cassegrain focus of ESO/MPG-2.2m telescope at La Silla, Chile. WFI (Baade et al. 1999) is a focal reducer-type mosaic camera which consists of  $4 \times 2$  CCD chips, each with  $2048 \times 4096$  pixels and a FOV of  $8.12' \times 16.25'$  ( $0.238''/\text{pixel}$ ). Chips are separated by gaps of  $23.8''$  and  $14.3''$  in the R.A. and Dec directions, respectively, so the WFI FOV is  $34' \times 33'$ , with a filling factor of 95.9%. The data presented here were obtained as part of a program carried out in visitor and service modes (P.I.: H. Böhringer) during MPG observing time. In particular, observations of RXCJ 0014.3-3022 and RXCJ 2308.3-0211 in the B, V, and R passbands were performed on September 27 through 30, 2000, and in photometric conditions. They were split into sequences of eight dithered sub-exposures. Total exposure times are listed in Table 1. Filter curves can be found in Arnouts et al. (2001) and on the web page of the La Silla Science Operations Team<sup>4</sup>. Standard stars were observed in all the four nights: three Landolt fields (Landolt 1992) were targeted for a total of 16 standard star OBs per filter.

<sup>4</sup> <http://www.la.silla.eso.org/lasilla/sciops/2p2/E2p2M/WFI/filters>

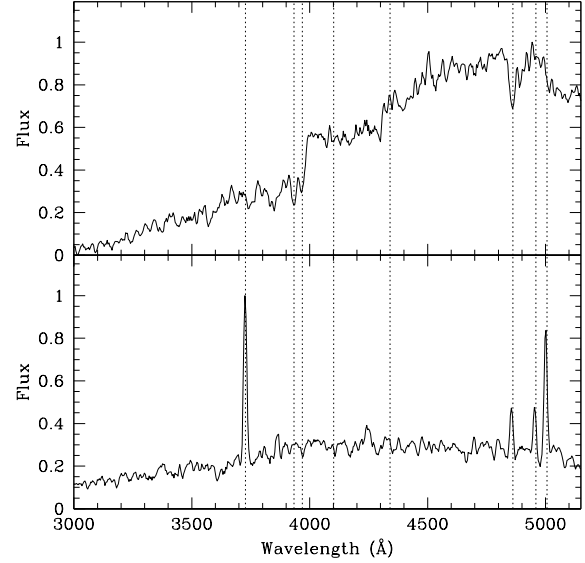


**Fig. 2.** Examples of VIMOS spectra (rest frame, normalised) for two members of RXCJ 2308.3-0211, with typical spectral features marked. Top: an elliptical galaxy, with Ca II<sub>H+K</sub> ( $\lambda\lambda$  3933.7, 3968.5 Å) absorption lines and H $\beta$  ( $\lambda$  4861.3 Å) feature in absorption. Bottom: an emission-line galaxy, with [O II] ( $\lambda$  3727.5 Å), H $\beta$ , and [O III] ( $\lambda\lambda$  4958.9, 5006.8 Å) emission features.

The WFI data were reduced using the data reduction system developed for the ESO Imaging Survey (EIS, Renzini & da Costa 1997) and its associated EIS/MVM image processing library version 1.0.1 (*Alambic*, Vandame 2004). *Alambic* is a publicly available<sup>5</sup> software designed to automatically transform raw images from single/multi-chip optical/infrared cameras into reduced images for scientific use. In addition to the standard bias-subtraction, flatfield correction, and trimming, the EIS/MVM image processing pipeline performs background estimation, de-fringing (if needed), astrometric calibration, minimisation of chip-to-chip variations in sensitivity, and detection/masking of satellite tracks. All these steps are described in detail in previous publications (Arnouts et al. 2001; Vandame 2004; Mignano et al. 2007; Pierini et al. 2008), and, thus, are skipped here. However, we note that the astrometric calibration was derived using the GSC2.2 reference catalogue and a distortion model described by a second order polynomial. Its precision is  $0.2''$  but the internal accuracy is about 70 mas (see Mignano et al. 2007). Furthermore, we note that the CCD-to-CCD gain variations were corrected using median background values sampled in sub-regions bordering adjacent CCDs, but no illumination correction was applied. This may lead to relative zeropoint offsets from the centre to the borders of the image of up to 10%, according to the *still experimental* method to derive a zeropoint correction map designed by Selman (2004).

Source detection and photometry were based on SExtractor (Bertin & Arnouts 1996) both for standard and science images. Magnitudes were calibrated to the Johnson-Cousins system using Landolt (1992) standard stars whose magnitudes were obtained using a 10 arcsec-wide circular aperture, which proved to be adequate by monitoring the growth curve of all the measured stars. Photometric standards were observed over a rather broad range of airmasses, but science frames were taken at the best air-

<sup>5</sup> [http://www.eso.org/science/eis/survey\\_release.html](http://www.eso.org/science/eis/survey_release.html)

mass per target; so the photometric solutions used to calibrate reduced images were obtained from merging all the measurements of standard stars for each passband. The number of non-saturated Landolt stars per field did not allow independent solutions to be determined for each of the eight chips of WFI. Hence calibration had to rely on solutions based on measurements taken across all chips. Despite the fact that the EIS data reduction system includes a photometric pipeline for the automatic determination of photometric solutions, these were determined interactively using the *IRAF*<sup>6</sup> task *fitparams*. This choice allows interactive rejection of individual measurements, stars, and chips. Photometric solutions with minimum scatter were obtained through a two-parameter linear fit to about 200 photometric points per passband, the extinction coefficient being set equal to that listed in the “definitive” solution obtained by the 2p2 Telescope Team<sup>7</sup>. In general, zeropoints and colour terms are consistent with those obtained by the 2p2 Telescope Team or by the ESO DEEP Public Survey (DPS) team (Mignano et al. 2007), as shown by the comparison of Tables 2, 3, and 4.

As for science images, source extraction and photometry were obtained after matching the BVR images of each target to the worst seeing (1 and 1.3'' FWHM for RXCJ 0014.3-3022 and RXCJ 2308.3-0211, respectively), using the *IRAF* task *psf-match*, and taking into account the weight-maps associated with the individual images, produced by *Alambic*. A common configuration file was used to produce three catalogues per target, a minimum number of trivial adjustments (e.g., seeing, zeropoint) being made for individual images. The deepest R-band image was used as the detection image, where sources are defined by an area with a minimum number of 5 pixels above a threshold of 1  $\sigma$  of the background counts. Source photometry in individual passbands was extracted in fixed circular apertures (from 1.2'' to 10'' in diameter) or in flexible elliptical apertures (Kron-like, Kron 1980) with a Kron-factor of 2.5 and a minimum radius of 3.5 pixels. Total magnitudes computed from the latter photometry (Kron-like) are used hereafter. Background subtraction was based on values taken directly from the background map, as obtained from a bi-cubic-spline interpolation, after applying median-filtering to sub-regions of an image equivalent to  $3 \times 3$  meshes, the mesh-size being equal to 64 pixels (i.e., 15.2''). Object magnitudes were corrected for galactic extinction according to the Schlegel et al. (1998) Galactic reddening maps (from *NED*) and converted to the AB system according to the response function of the optical system (see Alcalá et al. 2004). The output catalogues were successively pruned for fake sources by hand before photometric redshifts were determined. In addition, stars and galaxies could be safely identified on the basis of their surface brightness profile and optical colours down to  $R = 21.5$ . Fainter than this limit, number counts are dominated by galaxies, so that all detected objects with  $R > 21.5$  are assumed to be “bona fide” galaxies.

Depth and quality of the final catalogues were assessed in two ways. Firstly, we compared the number counts of stars safely identified in the R-band image of each cluster with those expected from the model of stellar population synthesis of the Galaxy by Robin et al. (2003) for  $R \leq 21.5$ . A good agree-

**Table 1.** The photometric solutions available in this work. The table lists: in Col. 1 the passband; in Cols. 2 – 4 the zeropoint in the Vega magnitude system (ZP), the extinction coefficient ( $k$ ), and the colour term (CT) together with their errors. These “best fit” parameters were obtained from a two-parameter fit to about 200 measurements across the WFI field for each passband, the extinction coefficient being fixed.

Passband	ZP	$k$	CT
B	$24.66 \pm 0.005$	0.22	$0.26 \pm 0.007$
V	$24.23 \pm 0.006$	0.11	$-0.15 \pm 0.012$
R	$24.50 \pm 0.007$	0.07	$-0.02 \pm 0.015$

ment between measured and expected values was found within the uncertainties. Secondly, we compared the number counts of galaxies, falling either within the entire mapped region of a cluster or in a low-density subregion (i.e., the “field”, see Sect. 3.3), with the galaxy number counts determined in deep fields (in particular VVDS Deep, McCracken et al. 2003). In general, our galaxy number counts exceed those obtained from observations of deep fields for  $R \leq 21.5$ , where our galaxies are safely identified (cf. Fig. 3). Unsurprisingly, this is especially true when the entire mapped regions of RXCJ 0014.3-3022 and RXCJ 2308.3-0211 are considered. On the other hand, the number counts of all galaxies, falling either in the “field” or in the entire mapped region of a cluster, start falling short of the galaxy number counts in deep fields at  $R = 22$ – $23$ . In particular, this deficit amounts to a factor of 2 at around 23.5 R-mag, where the number of background galaxies dominates the number of likely cluster members. Assuming as a completeness limit the magnitude at which the observed counts equal to 50% of the expected ones, we thus conclude that our R-band selected catalogues are complete down to  $\sim 23.5$  mag.

This holds in spite of the different decrease of number counts in the two cluster regions (see Fig. 3). The different behaviour at  $R > 23.5$  mag must be ascribed to a combination of Galactic absorption and seeing. In fact, RXCJ 0014.3-3022 lies in a sky region far away from the Galactic Plane and was observed at a typical seeing of  $\sim 1''$ ; conversely, RXCJ 2308.3-0211 lies close to the Galactic Plane and was observed at a typical seeing of  $\sim 1.2''$ . It is then likely that a larger fraction of objects fainter than  $\sim 23.5$  mag has failed detection in the second region. Consistently, catalogues exhibit comparable numbers of objects with  $R \leq 23.5$  mag: 14,409 for RXCJ 0014.3-3022 and 14,820 for RXCJ 2308.3-0211. A Kolmogorov-Smirnov test confirms that number counts for the two complete samples are consistent: the probability of a difference is equal to only 7.1%.

#### 2.4. GALEX UV photometry

In order to better constrain the recent star-formation activity in member galaxies of RXCJ 0014.3-3022 and RXCJ 2308.3-0211, we complemented the optical data with GALEX UV photometry. The GALEX data archive was scanned via the MultiMission Archive at Space Telescope Science Institute (MAST<sup>8</sup>): positions and total magnitudes of galaxies falling in the regions of both clusters were extracted from the All Sky Imaging Survey (GR3 data release). The total UV magnitude of an object was calculated as a weighted mean when multiple detections of the

<sup>6</sup> *IRAF* is the Image Reduction and Analysis Facility, a general purpose software system for the reduction and analysis of astronomical data. *IRAF* is written and supported by the *IRAF* programming group at the National Optical Astronomy Observatories (NOAO) in Tucson, Arizona. NOAO is operated by the Association of Universities for Research in Astronomy (AURA), Inc. under cooperative agreement with the National Science Foundation.

<sup>7</sup> <http://www.la.eso.org/lasilla/Telescopes/2p2T/E2p2M/WFI/zeropoints/>

<sup>8</sup> <http://galex.stsci.edu>



**Table 2.** The “definitive” photometric solutions obtained by the 2p2 Telescope Team from observations of standard stars in perfectly photometric nights, where a bunch of standard fields were moved around each chip of WFI. All parameters were fitted simultaneously as free parameters, with good airmass and colour range, and around 300 stars per fit. The table below gives the average solutions over all chips.

Passband	$ZP$	$k$	$CT$
$B$	$24.81 \pm 0.05$	$0.22 \pm 0.015$	$0.25 \pm 0.01$
$V$	$24.15 \pm 0.04$	$0.11 \pm 0.01$	$-0.13 \pm 0.01$
$R$	$24.47 \pm 0.04$	$0.07 \pm 0.01$	$0.00 \pm 0.00$

**Table 3.** The table below gives median values for all the photometric solutions based on three-parameter fits obtained by the ESO DPS team.

Passband	$ZP$	$k$	$CT$
$B$	24.58	0.22	0.24
$V$	24.23	0.19	-0.04
$R$	24.49	0.08	-0.01

same object exist from overlapping GALEX pointings. In general, cross-identification of GALEX sources with objects in our catalogues was largely unambiguous. When multiple catalogue objects were present within the radius of the GALEX PSF ( $6''$  FWHM), the bluest one (i.e., with smaller  $(B-R)$  colour) was identified as the counterpart of the UV source. In the absence of GALEX FUV detections,  $3\sigma$  upper limits on the UV magnitude are computed from the completeness FUV magnitude of the two fields imaged by GALEX.

### 3. Results

#### 3.1. Photometric redshifts

Cluster member galaxies are identified on the basis of photometric or spectroscopic redshifts; two catalogues are built accordingly. In the first case, member galaxies have photo- $z$ ’s consistent with the photo- $z$  of the cluster; hence they are “bona fide” members. In this section, it is described how we determine photometric redshifts, estimate their accuracy, and establish cluster membership based on photo- $z$ ’s.

Photometric redshifts are obtained by using a prior based on the  $(B-R)$  colour<sup>9</sup>, given the limited photometry available. This information is accurate enough only for objects brighter than the completeness limit of the photometric catalogues pruned for fake objects and stars brighter than  $R = 21.5$  (see Sect. 2.3). This is illustrated by the distribution of the errors on  $(B-R)$  as a function of  $R$ -band magnitude for the 23,900 objects in the region of RXCJ 0014.3-3022 with  $14 < R < 27$  (see Fig. 4). Objects brighter than  $R \sim 23.5$  exhibit a typical error on  $(B-R)$  of about 0.05 mag; only 248 objects among them (i.e., 0.02% of the complete sample) exhibit errors larger than 0.2 mag. The latter have  $21.4 < R \leq 23.5$ , with a mean  $R = 23.05$ .

<sup>9</sup> At the redshifts of the two clusters, the  $B$  and  $R$  broad-band filters map, respectively, the rest-frame wavelength ranges 3022–3940 Å and 4247–6045 Å. Hence, these two passbands bracket the 4000 Å break. In addition,  $B$  band contains the redshifted emission in the [OII] line.

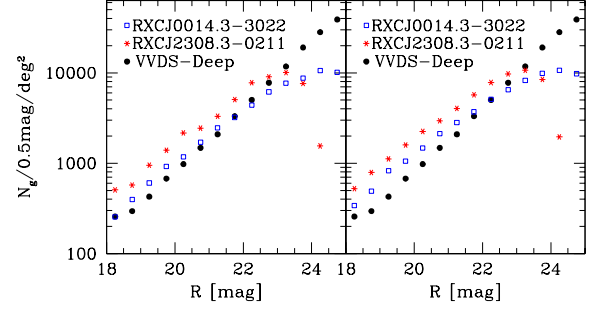


**Fig. 3.** Comparison of number counts for both clusters and the VVDS-Deep (McCracken et al. 2003). Left: number counts in a neighbouring, low density region of each cluster. Right: number counts for the entire region of a cluster imaged with WFI.

$(B-R)$  vs.  $R$  colour-magnitude (CM) diagrams are successively built from the complete catalogues of the two clusters, after removing some galaxies with photometry compromised by intervening bright stars. This action does not impact any of the following results. A visual inspection of both CM diagrams (see Fig. 5) clearly reveals the presence of a red sequence, which exhibits  $(B-R) \sim 2.2$  (observed frame). In each case, the red sequence was fitted using an iterative  $3\sigma$  clipping linear regression algorithm, all objects lying within a distance of  $3'$  from X-ray centroid of the cluster and with  $17 \leq R \leq 20$  being considered in the first step. The best-fits of the two red sequences are remarkably coincident, as shown later on. Thus objects in the complete samples of the two clusters are classified as “red” if they lie within  $3\sigma$  from the best-fit equation of the red sequence, or “blue” if their  $(B-R)$  colours are bluer than this locus at a significance higher than  $3\sigma$  (see Fig. 5).

This separation provides some guidance for selecting the SED templates that are explored to determine the photometric redshift of each object through the well-tested code *HyperZ* (Bolzonella et al. 2000). Specifically, red galaxies were only fitted using a suite of templates for galaxies dominated by old, passively-evolving stellar populations (E and S0 types), whereas blue objects were fitted with a suite of templates for star-forming galaxies (spirals and irregulars). Photometric redshifts were also determined without any prior on colour (i.e., morphology), which gave consistent results. Default synthetic non-evolving templates for E, S0, Sa, Sb, Sc, Sd, and Im galaxies were found to give the best results. Best-fit solutions from *HyperZ* were trained on spectroscopic redshifts, which provided an rms uncertainty of 0.06 at  $z = 0.3$  (see BPB07).

The photometric redshift of a cluster is defined as the mean of the photo- $z$ ’s of its spectroscopic members, as identified in Sect. 3.2. All galaxies with photo- $z$ ’s within  $\pm 1\sigma$  (i.e.,  $\pm 0.06$ ) from  $z_{\text{phot}}$  are defined as cluster photometric members.

##### 3.1.1. RXCJ 0014.3-3022: photometric members

The CM diagram of the inner region of RXCJ 0014.3-3022 shows that five galaxies populate a narrow bin ( $17.6 \leq R \leq 18.1$ ) at the bright-end of the red sequence. Four of them are part of two visual pairs of BCGs associated with the two X-ray sub-components of the cluster (see Pierini et al. 2008).

Fitting the CM distribution of 41 red-sequence objects, selected with a recursive algorithm, gives:

$$(B-R) = (2.935 \pm 0.238) - (0.037 \pm 0.003) \times R.$$

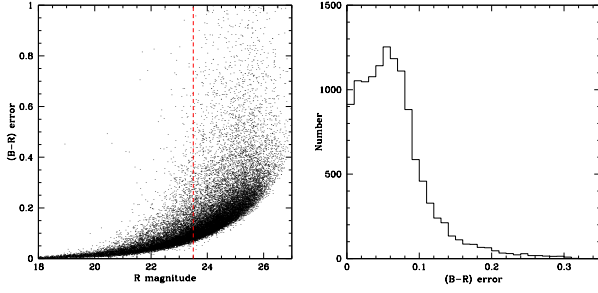


**Fig. 4.** Photometric quality of WFI data for RXCJ 0014.3-3022. Left: error on the  $(B-R)$  colour as a function of  $R$ -band magnitude ( $R$ ). A vertical dashed line marks the completeness limit  $R = 23.5$ . Right: distribution of errors on  $(B-R)$  for the complete sample.

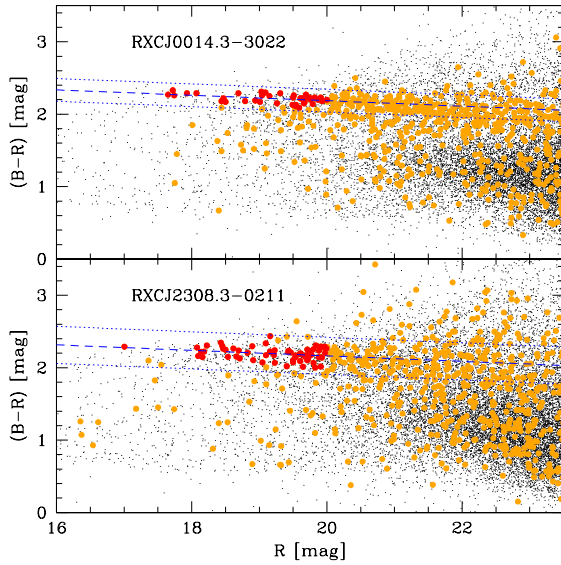


**Fig. 5.**  $(B-R)$  vs.  $R$  colour-magnitude diagram (observed frame) for the regions of RXCJ 0014-3022 (upper panel) and RXCJ 2308.3-0211 (lower panel) imaged with WFI. Orange points mark galaxies within  $3'$  from the cluster centre: most of them define a red-sequence. Red circles mark galaxies used for fitting the red sequence; this locus is reproduced (dashed line) together with the  $\pm 3\sigma$  scatter around it (dotted lines).

The rms scatter around this locus is equal to 0.052.

RXCJ 0014.3-3022 has  $z_{\text{phot}} = 0.34$  and its bona fide members have a photometric redshift between 0.28 and 0.4. Its photometric redshift is thus higher than the spectroscopic one ( $z = 0.3068$ ), although the two redshifts are consistent given the large typical uncertainty of photo- $z$ 's. The discrepancy is not driven by contamination from outliers, which is below 10%, or by the overall robustness of the identification of cluster members (see BPB07), but by blue members, which exhibit higher photo- $z$ 's and a larger scatter with respect to the red members, on average. This is mostly due to the presence of large peculiar velocities (up to  $4000 \text{ km s}^{-1}$ , see BPB07), which can produce a difference in  $z$  of up to  $\sim 0.02$ . The coupling of a relatively large, positive excess in the velocity along the line of sight and the rest-frame wavelength coverage offered by the filter set can boost photo- $z$ 's by about 0.04, but only for blue cluster member galaxies. In fact, at the cluster spectroscopic redshift, the red-

shifted [OII] emission line falls in the red tail of the B filter, and just shortwards of the blue edge of the V passband, whereas the  $4000 \text{ \AA}$  break falls in between the two passbands. The former feature characterises star-forming systems, the latter is stronger in old, passively evolving galaxies. Consistently, the photo- $z$ 's of red galaxies ( $\sim 0.32$ ) better agree with the spectroscopic redshift of the cluster.

In conclusion, the catalogue of photometric members of RXCJ 0014.3-3022 comprises 3698 galaxies across a 900 square arcmin-region centred at the X-ray centroid of the cluster, of which 1409 (2289) are classified as red (blue).

### 3.1.2. RXCJ 2308.3-0211: photometric members

The inner region of RXCJ 2308.3-0211 exhibits a similar red-sequence to that of RXCJ 0014.3-3022, but also three interesting differences. First, RXCJ 2308.3-0211 hosts a single BCG, which is brighter than other red photometric members by at least  $\sim 1$  R-mag. Second, its red-sequence is more populated (64 photometric members against 41) and exhibits a 60% larger RMS scatter (0.085 against 0.052). Third, red members amount to 57% of the total in RXCJ 2308.3-0211 against a value of 38% in RXCJ 0014.3-3022.

A fit to the red sequence defined by 64 robustly selected objects gives:

$$(B-R) = (2.933 \pm 0.323) - (0.038 \pm 0.003) \times R$$

with a scatter of 0.085. Photometric ( $z_{\text{phot}} = 0.29$ ) and spectroscopic ( $z = 0.2966$ ) redshifts are in excellent agreement for this cluster: thus, galaxies with photo- $z$ 's between 0.23 and 0.35 are identified as members. The catalogue of photometric members of RXCJ 2308.3-0211 contains 4109 objects across a 900 square arcmin-region centred at the X-ray centroid of the cluster, of which 2361 (1748) are classified as red (blue).

### 3.2. Spectroscopic redshifts

Spectroscopically confirmed members of either cluster are identified from the available spectroscopic catalogues as follows. As a first step, a relatively broad distribution in spectroscopic redshifts is considered, by selecting a range centred on the mean cluster redshift and with a width of 0.05. This is a fairly large value: it corresponds to a velocity range of about  $10,000 \text{ km s}^{-1}$  at  $z \sim 0.3$ . However, it avoids the “a priori” loss of high-speed cluster members and still enables unambiguous rejection of any other structure present in the foreground/background.

After this selection, cluster membership is estimated by using the biweight estimators introduced by Beers et al. (1990) and successively applied with success in many different studies (e.g. Biviano et al. 1992; Girardi et al. 1993; Adami et al. 1998; Girardi et al. 1998; Biviano et al. 2006). Successively, all objects with peculiar velocities larger than  $\pm 4000 \text{ km s}^{-1}$  are rejected. Interlopers are then removed following the algorithm of den Hartog & Katgert (1996, see also Katgert et al. 2004), which identifies galaxies unlikely to be bound to the cluster on the basis of their location in projected phase-space. Velocity errors and relativistic correction are applied to the cluster velocity dispersion estimate, as explained in Danese, De Zotti & di Tullio (1980). The X-ray centroid of each cluster was used as reference in these calculations. The application of the overall procedure is discussed in Braglia et al. (2009b, in prep.), whereas the method is validated by the analysis of clusters extracted from cosmological numerical simulations in Biviano et al. (2006).

Finally, each catalogue of spectroscopic cluster members is cross-correlated with the photometric one, which gives a new catalogue combining photometric and spectroscopic information. All detected spectroscopic targets are brighter than 23.5 R-mag, as expected. For this cross-correlation, the celestial coordinates of spectroscopic members were taken from pre-imaging. No correction for seeing was introduced since pre-imaging and R-band imaging were executed in similar seeing conditions. The catalogues of spectroscopic members for the two clusters are provided in Appendices B and C; they contain photometric information from WFI imaging as well as the spectral indices computed in Sect. 3.4.

### 3.2.1. RXCJ 0014.3-3022: spectroscopic members

The spectroscopic data reduction produced a total of 545 slits with at least one object in the entire region of RXCJ 0014.3-3022 covered with VIMOS. This corresponds to a total of 872 objects, since 147 slits contained multiple objects (up to 5). Among them, there are 64 serendipitous faint stars. For 262 objects, the S/N is too low for the extraction of a reliable spectrum, so they were flagged as non-detections. Out of the remaining 546 detected non-stellar objects, 43 were found to be multiple observations of the same galaxies. From these repeated observations, we estimate a mean velocity error equal to  $294 \pm 50 \text{ km s}^{-1}$ , which is in good agreement with the value of  $276 \text{ km s}^{-1}$  obtained for the VVDS using the same VIMOS instrumental setup. The error distribution for the corresponding pairs of spectroscopic redshift is plotted in Fig. 6. In conclusion, reliable VIMOS spectra are available for 512 non-stellar objects, which span the I-band magnitude range from 19 to about 22.5, and reach  $z = 0.85^{10}$ .

This sample was expanded by considering 101 additional objects in the field of RXCJ 0014.3-3022, selected from publicly available spectroscopic redshifts in *NED*. Cross-correlation of this new sample with our WFI photometric catalogue showed that the additional objects are mainly brighter than  $R = 22.0$  (see Fig. 7). Furthermore, 24 out of the 101 objects with spectroscopic redshifts in *NED* corresponded to objects at  $0.06 \leq z \leq 0.35$  and observed by us. Comparison of the photometric redshifts of the corresponding pairs allowed the external error of our redshift determinations to be assessed: it is equal to  $276 \pm 55 \text{ km s}^{-1}$ , on average, which is fully consistent with the internal error of the same measurements.

The final catalogue of spectroscopically confirmed members of RXCJ 0014.3-3022 comprises 190 different objects, 101 of which have VIMOS spectra. In the corresponding CM diagram, the red-sequence is visible (see Fig. 7); its fit, according to the same selection criteria as those used in Sect. 3.1.1, is:

$$(B - R) = (3.023 \pm 0.277) - (0.042 \pm 0.004) \times R.$$

The red sequence defined by spectroscopic members lying within  $3'$  from the centre of RXCJ 0014.3-3022 and with  $17 \leq R \leq 20$  exhibits a slightly higher normalisation and RMS scatter (0.049), together with a slightly steeper slope, than the locus defined by analogous photometric cluster members. Differences are not statistically significant however.

Finally, we note that there are three very blue objects (i.e., with  $(B - R) \leq 1$ ) even in the inner region of RXCJ 0014.3-3022, i.e., within a cluster-centric distance of about 800 kpc. This is consistent with the presence of enhanced star-formation activity even there, as found by Couch et al. (1998) and BPB07, although phase-space projection effects cannot be completely ruled out.

<sup>10</sup> Three quasars at  $z = 1.02, 2.51$ , and  $3.08$  were also detected.

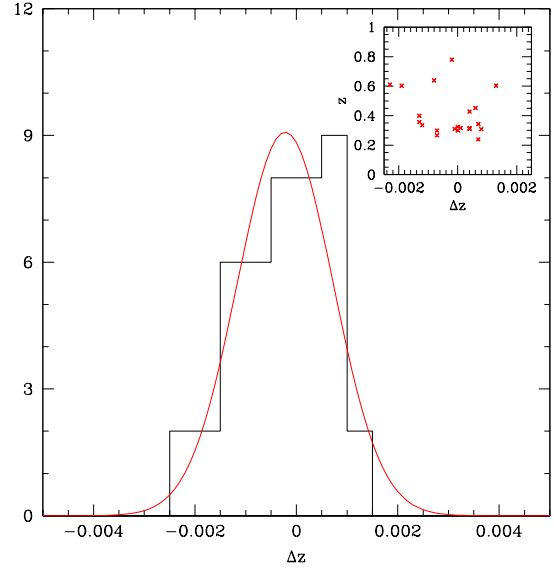


**Fig. 6.** Distribution of the errors on spectroscopic redshifts for multiply-observed galaxies in the region of RXCJ 0014.3-3022. In the main plot, a gaussian fit to this distribution is also reproduced. In the upper right inset, the same errors (in abscissa) are plotted against the associated redshifts. No clear correlation is found for these galaxies, which mostly lie at the same redshift of the cluster.

### 3.2.2. RXCJ 2308.3-0211: spectroscopic members

For the region encompassing RXCJ 2308.3-0211, a total of 1122 slits is available from our VIMOS spectroscopy. They provide 1522 spectra, since 424 slits contained multiple objects: 64 spectra correspond to faint stars, whereas 446 have a too poor S/N. As a result, 1012 spectra of non-stellar objects were collected, which span the redshift range  $0 \leq z \leq 0.85^{11}$ , of which 104 result to be multiple observations. This gives an intrinsic error on spectroscopic redshifts equal to  $254 \pm 49 \text{ km s}^{-1}$ , in good agreement with our previous determination and the VVDS one (cf. Sect. 3.2.1). In conclusion, the catalogue of VIMOS galaxy spectra in the region of RXCJ 2308.3-0211 is made of 902 robustly identified objects. No additional spectroscopic redshifts were found in *NED*.

According to the procedure of assigning cluster membership previously described, the final catalogue of spectroscopically confirmed members of RXCJ 2308.3-0211 comprises 269 galaxies. The fit of the corresponding red-sequence members gives:

$$(B - R) = (3.026 \pm 0.748) - (0.043 \pm 0.013) \times R. \pm 0.114$$

Comparison of the analogous loci defined by photometric or spectroscopic members of RXCJ 2308.3-0211 confirms the behaviour found for RXCJ 0014.3-3022. The same holds for the comparison of fits obtained for the two clusters. Therefore, the fit of the photometric members of the red sequence of either cluster will be used hereafter, as this is based on larger statistics.

No spectrum exists for the BCG of RXCJ 2308.3-0211, which sits at the cluster centre (Pierini et al. 2008). Interestingly, there is a spectroscopic member with about 60% of the R-band luminosity of the BCG (see Fig. 7). It lies at a cluster-centric distance of  $55''$  (i.e. about 240 kpc at the cluster's redshift) from

<sup>11</sup> Six quasars at  $z = 1.09, 1.32, 2.01, 2.04, 2.14$ , and  $3.16$  were also detected.



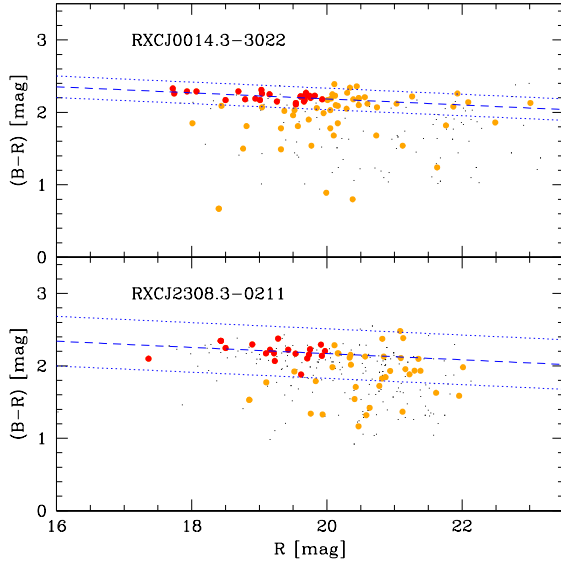


**Fig. 7.** The same as in Fig. 5 but for the spectroscopic members of each cluster. The red sequences defined by either spectroscopic or photometric members lying within  $3'$  from the centre of each cluster are identical.

the cluster centre; it was not considered in the analysis made by the previous authors.

### 3.3. Cluster morphology: hot gas vs. galaxies

The available X-ray surface brightness distributions (Zhang et al. 2006), which witness the dynamical state of the hot gas (Jones & Forman 1992), are complemented with surface density maps of member galaxies for the two clusters, determined as described in Appendix A. Comparison of the two-dimensional distributions of hot gas and galaxies improves our knowledge about substructure and large-scale structure in and around the clusters.

The entire population of photometric member galaxies of a cluster and its red and blue subpopulations are considered separately. In all three cases, the same smoothing for the enhancement of structure against a smooth background and final spike cleaning is used, which consists in a gaussian kernel of  $100''$ . Galaxy density maps were always extracted with the same resolution (mesh width of  $10''$ ) to directly compare results. Spectroscopic catalogues were considered as well, although they cover only a fraction of the region imaged with WFI. In this case, the mesh width and smoothing scale have been increased to  $20''$  and  $250''$ , respectively, to compensate for the poorer statistics, and, thus, to ensure convergence and avoid occurrence of spikes produced by undersampling. Table 4 gives results from the calculation of the smooth background calculation for all catalogues used. In all cases, the RMS value of the smooth background is used as standard unit to estimate the overdensity associated with a given structure.

#### 3.3.1. RXCJ0014.3-3022

The complex morphology of RXCJ0014.3-3022 at different scales was illustrated by Böhringer et al. (2006) and BPB07, with different tracers and techniques. In particular, there is evidence for two extended filamentary structures of galaxies stemming out of the main body of this merging cluster, one heading to

catalogue	N. objects	Mean BG	RMS
RXCJ0014.3-3022 (all)	3698	32.37	10.31
RXCJ0014.3-3022 (red)	1409	9.70	4.28
RXCJ0014.3-3022 (blue)	2289	21.91	6.90
RXCJ0014.3-3022 (spec.)	190	1.90	3.03
RXCJ2308-0211 (all)	4109	44.72	14.74
RXCJ2308-0211 (red)	2361	23.26	9.52
RXCJ2308-0211 (blue)	1748	20.10	7.52
RXCJ2308-0211 (spec.)	269	1.18	5.01

**Table 4.** Background evaluation results for the different subcatalogues of cluster members, for both clusters. Values are always given in units of number of galaxies per square Mpc.

the North-West (NW), the other to the South (S). Here we use the same subregions identified in BPB07, i.e.: the cluster core, the two filaments, and a neighbouring, low-density region assumed to represent the coeval “field” environment unaffected by the cluster. The statistics of the field is used to determine significant overdensities. The geometrical criteria (in addition to those on observed magnitude and photo- $z$ ) behind the definition of each subregion (and corresponding subcatalogue) are listed in Table 5. There the criteria are expressed as local polar coordinates with respect to the cluster centre, with the cluster-centric distance expressed in arcminutes, the polar angle in degrees (with the zero angle towards E and increasing counterclockwise w.r.t. the observer) and the enclosed area in square arcminutes.

The main body of RXCJ0014.3-3022 is elongated in the NW-SE direction, which is where the two main clumps of galaxies lie, but it also exhibits lots of scattered extensions. The most outstanding ones are the two filaments to the NW and S, which can be traced out to about  $9'$  (i.e., 2.44 Mpc) and certainly extend beyond the imaged region of the cluster, and, thus, beyond the X-ray  $R_{200}$  (2.52 Mpc, Zhang et al. 2006). These two elongated structures host about the same number of galaxies, and as many as the core, which occupies an area four times smaller though. However, the S filament stands out more clearly as a twisted chain of high-density lumps, whereas the NW filament appears as a smoother distribution of slightly overdense peaks (see Fig. 8). Unsurprisingly, red galaxies highlight the main body of the cluster, but they also trace the inner part of the filaments. In addition to the two central clumps each associated with BCG pairs (see Pierini et al. 2008), a third, less dense clump of red galaxies lies slightly to the N w.r.t. the cluster centre: it hosts a fifth BCG, as anticipated (see Sect.3.2.2). An additional overdensity of red galaxies (w.r.t. to the field) lies to the SE; it appears as detached from the main body of the cluster.

The overall picture is confirmed by the distribution of the spectroscopically confirmed cluster members. Although the available spectroscopy does not extend to the outer edges of the filaments, at least the inner part of the S filament is traced by spectroscopic cluster members. Remarkably the same conclusion can be reached from the X-ray surface brightness distribution (Fig. 8) and entropy map (Böhringer et al. 2006) of the hot gas. Unsurprisingly, filaments are better traced by blue galaxies. Nevertheless, an overdensity of blue galaxies (w.r.t. the field) lies exactly between the three clumps of red galaxies associated with BCGs previously described. Its presence is consistent with the findings of Couch et al. (1998). In addition, two regions with a less marked overdensity of blue galaxies are discovered: they just trail the two main clumps of red galaxies in the main body of the cluster. One of them is led by an X-ray bow-shock detected with *Chandra* (see Kempner & David 2004) and associated with the NW subcomponent of this merging cluster. As discussed in

Region	Radius	Angle	Objects	Area
Cluster core	$0' \leq r \leq 3'$	$0 \leq \theta \leq 360$	304	$9\pi$
NW filament	$3' < r \leq 15'$	$-10 \leq \theta \leq 50$	359	$36\pi$
S filament	$3' < r \leq 15'$	$260 \leq \theta \leq 320$	374	$36\pi$
BG field	$6' < r \leq 18'$	$120 \leq \theta \leq 210$	488	$72\pi$

**Table 5.** Definition of regions of interest in RXCJ0014.3-3022. Areas are expressed in square arcminutes.

Region	Radius	Angle	Objects	Area
Cluster core	$0' \leq r \leq 3'$	$0 \leq \theta \leq 360$	258	$9\pi$
Inner outskirts	$3' < r \leq 6'$	$0 \leq \theta \leq 360$	293	$27\pi$
Outer outskirts	$6' < r \leq 9'$	$0 \leq \theta \leq 360$	429	$45\pi$
BG field (1)	$9' < r \leq 19'$	$200 \leq \theta \leq 240$	255	$31.1\pi$
BG field (2)	$9' < r \leq 19'$	$300 \leq \theta \leq 350$	228	$38.9\pi$

**Table 6.** Definition of regions of interest in RXCJ2308.3-0211. Areas are expressed in square arcminutes.

BPB07, this shock may shield infalling galaxies from the surrounding ICM, which enables them to continue their normal star formation activity.

### 3.3.2. RXCJ 2308.3-0211

In X-rays RXCJ 2308.3-0211 appears as an azimuthally symmetric, centrally concentrated system, as typical of cool-core clusters. For the region of this cluster we define five subregions (see Table 6): the cluster core, two outer, concentric circular annuli, and two low-density regions (i.e., “fields”). We note that the total circular area occupied by the cluster, defined as the sum of the core and the two annular regions, contains 980 galaxies within a radius of  $9'$ . For comparison, RXCJ 0014.3-3022 hosts 1016 galaxies within the same cluster-centric distance. Furthermore, the total area of the field regions for RXCJ 2308.3-0211 is equivalent to the area of the field for RXCJ 0014.3-3022; it also contains the same number of objects.

Consistently with the cool-core nature of the cluster, the distribution of red galaxies is centrally concentrated, the BCG itself sitting at the cluster centre. However, the optical morphology of the cluster is not regular, as confirmed by the two-dimensional distribution of spectroscopic cluster members. Furthermore, two pronounced overdensities of red galaxies lie to the N of RXCJ 2308.3-0211, about  $15'$  (i.e.,  $\sim 4.1$  Mpc) away from it. They are well beyond the X-ray  $R_{200}$  of the cluster (2.44 Mpc; Zhang et al. 2006) and are separated by  $\sim 4'$  (i.e., about 1.2 Mpc). These two structures are likely groups at the same redshift of RXCJ 2308.3-0211; they seem to be detected in X-rays as well, although they lie at the edge of the XMM-Newton image. Both the red galaxy density distribution and the two-dimensional distribution of spectroscopic cluster members suggest the existence of a bridge between these two groups and RXCJ 2308.3-0211. This also compares well with the weak lensing analysis in Dahle et al. (1980), where the mass distribution is seen to be elongated towards N. An additional overdensity of spectroscopic members eastwards of the main cluster finds correspondence in the red galaxy map and in the X-ray image. A Dressler–Schechtman analysis (Dressler & Schechtman 1988) suggests that this structure is likely a group which is still not connected to the cluster (Braglia et al. 2009b, in prep.). Finally, there are extremely few overdense structures traced by blue galaxies, across the WFI image: the main ones form a sequence of blobs jutting out of the cluster centre in the NE direction.

### 3.4. Spectral indices: global behaviour of galaxy populations

The strength of the 4000 Å break ( $D4000$ ) and the equivalent widths of the  $H_\delta$  photospheric absorption line and the [OII] nebular emission line ( $W_0(H_\delta)$  and  $W_0([OII])$ , respectively) could be robustly determined from VIMOS spectra with  $S/N > 4$  for galaxies at  $z \sim 0.3$ . An analysis based on these spectral features can constrain the star-formation histories of individual cluster members (e.g. Balogh et al. 1999; throughout this paper we will use the same definition adopted in there, where  $W_0([OII])$  is positive when in emission and  $W_0(H_\delta)$  is positive in absorption). In fact, the spectral index  $D4000$  is particularly sensitive to the presence of old (i.e.,  $\geq 1-2$  Gyr), passively evolving stellar populations. Conversely,  $W_0(H_\delta)$  is sensitive to episodes of star formation in the last Gyr, since it measures the presence of A-type stars, whereas  $W_0([OII])$  estimates the present star formation activity (i.e., the SFR on timescales of  $\leq 0.01$  Gyr). The combined use of the diagnostic diagrams  $W_0(H_\delta)-W_0([OII])$  and  $W_0(H_\delta)-D4000$  limits misinterpretations arising from non introducing corrections for intrinsic extinction by dust or additional line emission affecting  $W_0([OII])$  and  $W_0(H_\delta)$ , respectively.

The behaviour of each spectral index as a function of the observed  $(B-R)$  colour (uncorrected for internal extinction) for the spectroscopic members of each cluster is reproduced in Fig. 10. Unsurprisingly, galaxies with redder  $(B-R)$  colours tend to exhibit lower values of  $W_0([OII])$  (i.e., less emission in the [OII] line) and larger values of  $D4000$ . Hence, they have experienced less star-formation activity since the last Gyr or so, and, thus, tend to be dominated by old, passively evolving stellar populations. Interestingly, this holds irrespectively of the galaxy luminosities.

In analogy with previous spectral index analyses (e.g. Barger et al. 1996; Balogh et al. 1999), we empirically determine threshold values for the three spectral indices in order to discriminate different star-formation regimes. In particular, red sequence galaxies identified photometrically (cf. Sect. 3.1 and 3.2) are used to determine mean and RMS of  $W_0([OII])$ ,  $W_0(H_\delta)$ , and  $D4000$  that are assumed to represent galaxies dominated by old, passively evolving stellar populations. These are defined as the objects falling within  $3\sigma$  from the mean of  $W_0([OII])$  or  $D4000$ , which operationally translates into:  $W_0([OII]) < 4.85 \text{ \AA}$  in the  $W_0([OII])-W_0(H_\delta)$  diagnostic diagram, or  $D4000 \geq 1.4$  in the  $D4000-W_0(H_\delta)$  one. These thresholds are well consistent with those adopted by Balogh et al. (1999) or Dressler et al. (1999), according to their samples and data (i.e.,  $W_0([OII]) = 5 \text{ \AA}$  and  $D4000 = 1.45$ , respectively). Following these authors, we adopt  $W_0(H_\delta) = 0 \text{ \AA}$  as a threshold between normal star-forming and (short) starburst galaxies.

In absence of detected objects with extreme values of  $W_0(H_\delta)$  in our samples, the spectroscopically confirmed member galaxies of our clusters belong to one of the following three classes (see also Tables 7 and 8; cf. Balogh et al. (1999)).

*Passive galaxies (PEV):* systems currently not undergoing traceable star formation activity, mainly with E or S0 spectral type (and morphology). They are defined by  $W_0(H_\delta) \leq 5 \text{ \AA}$  and  $W_0([OII]) < 4.85 \text{ \AA}$ , or  $D4000 \geq 1.4$ .

*Star-forming galaxies (SF):* systems undergoing significant star formation activity since at least several hundred million years, mainly identified as late-type galaxies (spirals and irregulars). They are identified by  $0 \leq W_0(H_\delta) \leq 5 \text{ \AA}$  and  $W_0([OII]) \geq 4.85 \text{ \AA}$ , or alternatively  $D4000 < 1.4$ .

*Short starburst galaxies (SSB):* systems currently undergoing a short-lived, intense episode of star formation (i.e.,  $\leq 200$

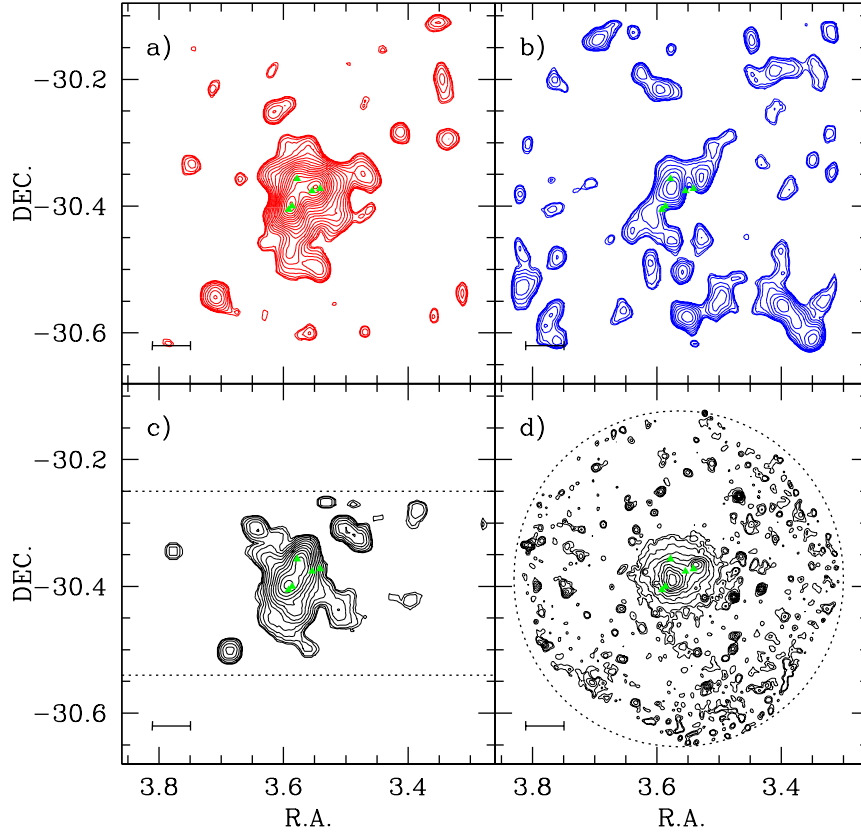


**Fig. 8.** Galaxy density maps and X-ray image for RXCJ 0014.3-3022. Panels a) and b) show, respectively, the density maps of red and blue photometric members. Panel c) shows the density map of spectroscopic members instead, where dotted lines mark the approximate extent of the VIMOS combined pointings. Panel d) shows the distribution of the X-ray emitting, hot gas, where a dotted circle marks the approximate FOV of XMM-Newton. Green triangles mark the positions of the BCGs of every galaxy clumps. In all maps, reproduced contours have a significance of at least  $5\sigma$  w.r.t. the background. The lower left horizontal bar has a size of 1 Mpc at the cluster’s redshift.

Myr), where nebular emission is strong. They have  $W_0(H_\delta) < 0 \text{ \AA}$  and  $W_0([OII]) \geq 4.85 \text{ \AA}$ , or alternatively  $D4000 < 1.4$ .

Although none of the cluster members fall into the following definition, we want to define here an additional class which will be useful in our analysis, the so-called *post-starburst galaxies* (Dressler and Gunn 1983; Poggianti et al. 1999). These systems show negligible emission lines but strong Balmer absorption; this suggests that star formation activity in these systems ended abruptly in the recent past. According to Poggianti et al. (1999) and our previous definitions, we define these systems as having  $W_0(H_\delta) \geq 5 \text{ \AA}$  and  $W_0([OII]) < 4.85 \text{ \AA}$ .

The diagnostic diagrams  $W_0([OII])$ – $W_0(H_\delta)$  and  $D4000$ – $W_0(H_\delta)$  establish that RXCJ 0014.3-3022 and RXCJ 2308.3-0211 host overall different galaxy populations (see Fig. 11). In fact, a diagnostic two-dimensional Kolmogorov-Smirnov test (Fasano & Franceschini 1987; Peacock 1983), executed for the distribution of members of either cluster in the two previous diagnostic diagrams, concludes that the probability that the two distributions are drawn from the same parent population is absolutely negligible: 0.02% for the  $D4000$ – $W_0(H_\delta)$  plane, and 0.41% for the  $W_0([OII])$ – $W_0(H_\delta)$  plane. The very significant difference between the galaxy populations of the two clusters is not due to selection effects, since the selection function of spectroscopic targets was the same (cf. Sect. 2.2).

This is confirmed by the different distribution of spectroscopic cluster members in the  $D4000$ – $(FUV - V)$  colour (rest frame<sup>12</sup>) plane (cf. Moran et al. 2007), as shown in Fig. 12. There galaxies are flagged as passive or star-forming according to their values of  $W_0([OII])$ . Out of 101 (269) spectroscopic members of RXCJ 0014.3-3022 (RXCJ 2308.3-0211), 12 (7) were detected by GALEX in the FUV<sup>13</sup>. It is evident that not only the fraction of FUV-detected member galaxies, but also the overall distribution of member galaxies with lower limits on  $(FUV - V)$  is different. In particular, the bulk of spectroscopic members of RXCJ 2308.3-0211 does not exhibit  $(FUV - V) < 2$  (rest frame), whatever the value of  $D4000$ , whereas RXCJ 0014.3-3022 hosts a non-negligible population of galaxies with  $D4000 < 1.6$  and  $(FUV - V) < 2$ . We attribute the strong differences in galaxy populations between RXCJ 0014.3-3022 and RXCJ 2308.3-0211 to the largely different dynamical states and morphologies of the two clusters (see Sect. 3.3 and Braglia et al. 2009b, in prep.).

<sup>12</sup> GALEX FUV and WFI V-band magnitudes of individual objects are  $k$ -corrected according to the best-fit templates in *HyperZ*.

<sup>13</sup> Most of the FUV-detected galaxies in RXCJ 0014.3-3022 lie close to the cluster core and in the region of the S filament, in correspondence of the clumps of blue galaxies discussed in Sect. 3.3.

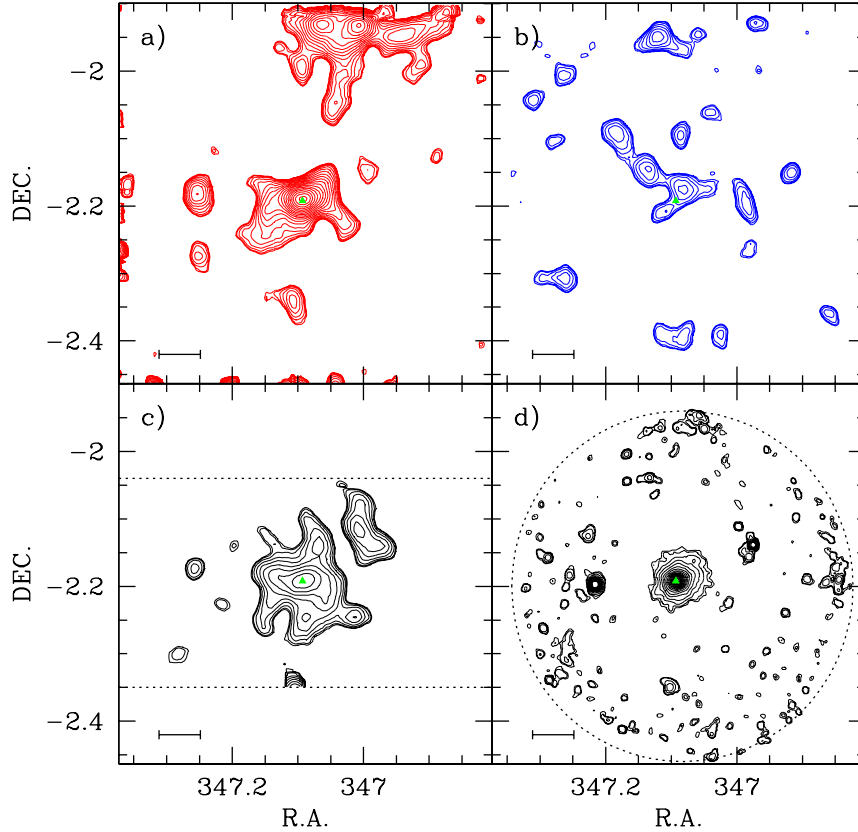


**Fig. 9.** The same as in Fig. 8 but for RXCJ 2308.3-0211.

**Table 7.** Definitions in the  $[W_0(OII), W_0(H_\delta)]$  plane

Definition	$W_0(OII)$	$W_0(H_\delta)$
PEV (passive)	$< 4.85$	$\leq 5$
SF (star-forming)	$\geq 4.85$	$\in [0, 5]$
SSB (short starburst)	$\geq 4.85$	$< 0$

Finally, we note that both clusters host a small but odd population of galaxies with  $(B - R) \geq 2$  and either  $D4000 < 1.4$  or  $W_0([OII]) \geq 4.85 \text{ \AA}$ . In RXCJ 0014.3-3022 these few objects are sub- $L^*$ , whereas there are some luminous ones in RXCJ 2308.3-0211. We tentatively interpret this odd class of red galaxies with evidence of recent or present star-formation activity as dusty galaxies with very different SFRs (cf. Verdugo et al. 2008). They are not post-starburst galaxies though, since they do not show a large absorption in the  $(H_\delta)$  line (i.e.  $\geq 5$ ). There is now substantial observational evidence from IR observations that cluster galaxies can experience strongly obscured star-formation activity (e.g. Metcalfe et al. 2005; Saintonge et al. 2008, and references therein). This population of dust-obscured star-forming galaxies seems particularly abundant in galaxy clusters undergoing merging and strong episodes of mass accretion (e.g. Coia et al. 1999; Tran et al. 2005; Loh et al. 2008), with little dependence on the mass of the parent system as they are also observed in groups (Wilman et al. 2008). A large fraction of these dusty galaxies are classified as early-type spirals (e.g. Biviano et al. 2004; Wilman et al. 2008), in agreement with the average spectral type of our red, star-forming population.

**Table 8.** Definitions in the  $[D4000, W_0(H_\delta)]$  plane

Definition	$D4000$	$W_0(H_\delta)$
PEV (passive)	$\geq 1.4$	$\leq 5$
SF (star-forming)	$< 1.4$	$\in [0, 5]$
SSB (short starburst)	$< 1.4$	$< 0$

### 3.5. Spectral indices: local behaviour of galaxy populations

Here we investigate if differences in galaxy populations between RXCJ 0014.3-3022 and RXCJ 2308.3-0211 arise in well defined regions of the two clusters. Firstly, we analyse the behaviour of the spectral indices of spectroscopically confirmed members as a function of the cluster-centric distance (see Fig. 13). In RXCJ 0014.3-3022, spectroscopic members tend to exhibit  $D4000 < 1.4$  when their cluster-centric distances approach or exceed the value of  $R_{200}$ . The increase of the fraction of star-forming systems towards and beyond  $R_{200}$  is confirmed by the corresponding behaviours of  $W_0([OII])$  and  $W_0(H_\delta)$ . This is consistent with the existence of a sharp peak in the fraction of blue-to-red galaxies along the two filaments (see BPB07) especially the southern one, which is poorly sampled by the available VIMOS data (see Fig. 1). Conversely, the combined behaviour of the same spectral indices for spectroscopic members of RXCJ 2308.3-0211 as a function of cluster-centric distance shows that passive galaxies dominate everywhere in this cluster. Furthermore, luminous galaxies (i.e., with  $L_R \geq L_R^*$ ) tend to be passive already beyond  $R_{200}$  in RXCJ 2308.3-0211, whereas passive, luminous galaxies almost exclusively populate regions



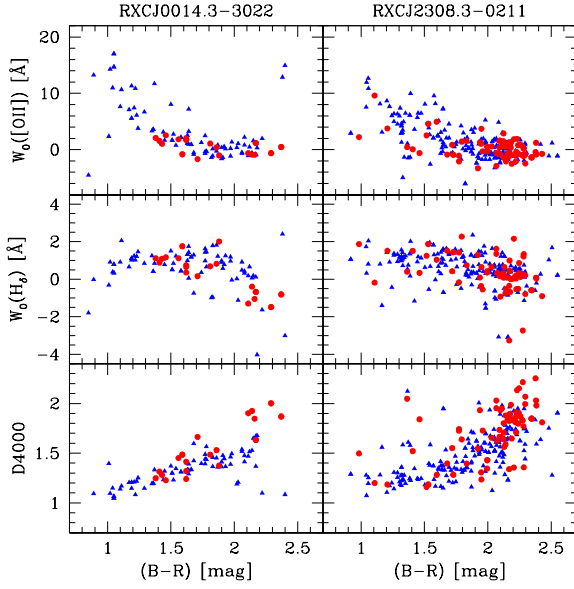


**Fig. 10.** Spectral indices  $W_0(H_\delta)$ ,  $W_0([OII])$ , and  $D4000$  (see text) as a function of  $(B - R)$  colour (observed frame) for spectroscopic members of RXCJ 0014.3-3022 (left column) and of RXCJ 2308.3-0211 (right column). Triangles and circles mark sub- $L^*$  (i.e., with  $L_R < L_R^*$ ) and luminous galaxies, respectively.

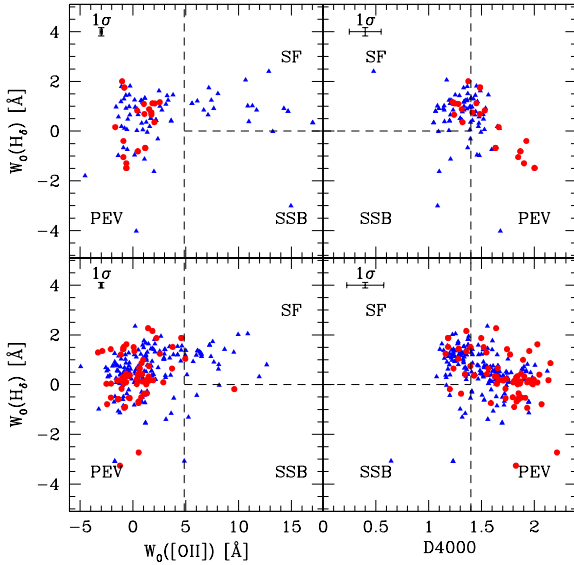


**Fig. 11.** Spectral index diagnostic diagrams for spectroscopic members of RXCJ 0014.3-3022 (top row) and of RXCJ 2308.3-0211 (bottom row). In each panel, symbols are the same as in Fig. 10, whereas dashed lines mark thresholds for discriminating different star-formation regimes (see Tables 7 and 8). Symbols are the same as in Fig. 10.

within  $R_{200}$  in RXCJ 0014.3-3022. Analogous differences exist when considering the population of sub- $L^*$  galaxies in the two clusters. This suggests that galaxies already tend to be passive and, thus, populate the red sequence only outside the virialized region in RXCJ 2308-0211, in agreement with previous findings for other clusters (Kodama et al. 2001, 2003; Balogh et al. 1997). In particular, Balogh et al. (1997) found that star formation in

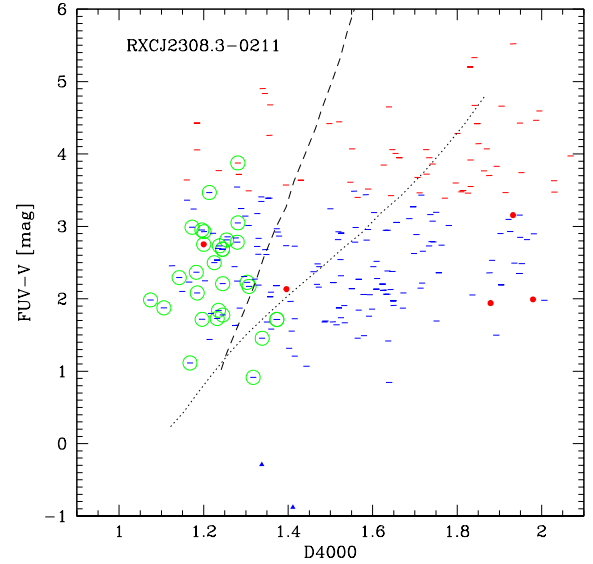
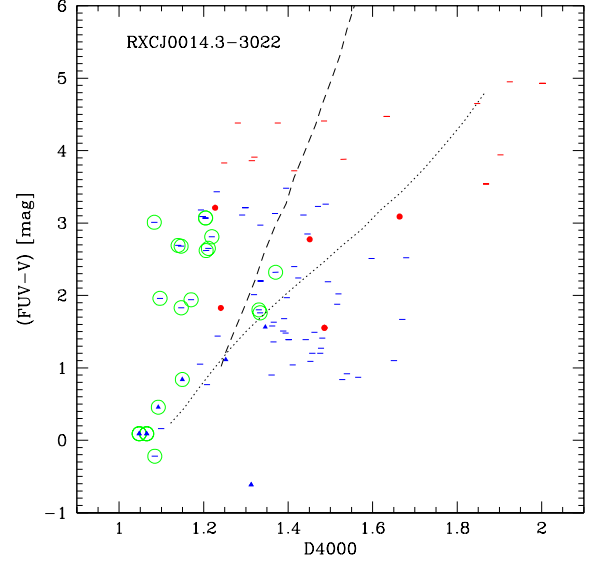


**Fig. 12.** Rest-frame  $(FUV - V)$  colour as a function of  $D4000$  for the spectroscopic members of RXCJ 0014.3-3022 (top) and of RXCJ 2308.3-0211 (bottom). In each panel, symbols are the same as in Fig. 10. In addition, red and blue bars mark lower limits on  $(FUV - V)$  for luminous and sub- $L^*$  galaxies, respectively. Furthermore, green circles mark galaxies with significant  $[OII]$  emission (i.e.,  $W_0([OII]) \geq 4.85 \text{ \AA}$ ). Finally, dashed and dotted lines mark, respectively, models corresponding to a star-formation or a truncation evolutionary track, similarly to Moran et al. (2007).

cluster galaxies is generally suppressed (w.r.t. the field) out to  $2R_{200}$ . Conversely, galaxies tend to mostly populate the red sequence inside the virialized region in RXCJ 0014.3-3022.

To better understand these differences, we investigate subregions of the two clusters as well as their neighbouring fields. As for RXCJ 0014.3-3022 (Fig. 14), spectroscopic members in the core region are mostly passive at variance with the galaxy population in the neighbouring field. This contains a mixture of passive and mildly-to-highly star-forming systems. Nevertheless, there is additional evidence of the presence of (mostly faint)

galaxies with intense star-formation activity in the cluster core (see Couch et al. 1998). Spectroscopic members associated with the two filaments of RXCJ 0014.3-3022 exhibit properties in between those of the galaxy populations in the cluster core and the neighbouring field. Unfortunately, the present VIMOS data do not extend much beyond  $R_{200}$  in the direction of the S filament, where most of the “flaming giants” discovered by BPB07 lie.

As for RXCJ 2308.3-0211, the star-formation activity of spectroscopic members appears as low everywhere, but tend to increase towards  $R_{200}$  (cf. Fig. 13, right panel). Consistently,  $D4000$  tends to decrease from the core to the outskirts of the cluster. Star-formation activity appears to be almost exclusively present in sub- $L^*$  galaxies. This picture is in agreement with previous results in the literature (e.g. Balogh et al. 1999). However, the paucity of star-forming galaxies, not only among the luminous ones, is evident also in the neighbouring field.

#### 4. Discussion

RXCJ 0014.3-3022 and RXCJ 2308.3-0211 are two clusters at  $z \sim 0.3$  with comparable X-ray luminosities<sup>14</sup> (thus, likely, total masses), but with opposite X-ray morphologies (i.e., dynamical states): the former is a merging system, the latter a regular, centrally concentrated one. The optical morphologies of both clusters are more complex than the X-ray ones. In addition to the two X-ray subcomponents, RXCJ 0014.3-3022 exhibits two extended filaments (one of which is tentatively detected in X-rays) and a core rich in substructure, as traced by galaxies with photometric or spectroscopic redshift consistent with that of the cluster. Furthermore, its core hosts two visual pairs of BCGs, each associated with a displaced X-ray subcomponent (see Pierini et al. 2008 for a discussion), and an additional equally luminous BCG sitting in a third overdense region. On the other hand, the X-ray centroid of RXCJ 2308.3-0211 coincides with the position of its BCG, as expected for a cool-core cluster, but photometric or spectroscopic cluster members shape a core region which is less centrally symmetric than in X-rays. The difference between optical and X-ray shape can be well explained in terms of the different properties of the various cluster components. The gas particles have isotropic motions, thus follow isopotential contours which are smoother than the distribution of galaxies and dark matter, which instead show non-isotropic velocity distributions. Moreover, the X-ray surface brightness follows the projected square density of the gas and thus emphasises the more regular central region, mainly missing the irregular outskirts where the gas density is low.

In spite of the evident difference in assembly state at  $z \sim 0.3$ , these clusters exhibit the same locus of galaxies dominated by old, passively evolving stellar populations<sup>15</sup>. The red sequence of each cluster is well populated, whether it is traced by photometric or spectroscopic members.

However, the star-formation history of the average galaxy is quite different for the two clusters, as confirmed by their spectroscopic members. Combining information from the distributions of these galaxies in the  $W_0([OII])$ – $W_0(H_\delta)$ ,  $D4000$ – $W_0(H_\delta)$ , and  $D4000$ – $(FUV - V)$  planes<sup>16</sup> offers the consistent picture that star-formation activity is rapidly moving towards a quiescent state, if it is not already absent, across the virialized

region of RXCJ 2308.3-0211, whatever the R-band luminosity of its spectroscopic members. This is confirmed by comparison of the distributions in the  $D4000$ – $(FUV - V)$  plane of real galaxies and models corresponding to evolutionary scenarios for either starvation or (abrupt) truncation of the star-formation activity (Moran et al. 2007). In both clusters, we recover the standard scenario that the overall stellar population in galaxies tends to become younger towards the outskirts (e.g. Balogh et al. 1999). In RXCJ 2308.3-0211, this is mostly due to (residual) star-formation activity in sub- $L^*$  galaxies, since even the neighbouring field contains galaxies with  $L_R \geq L_R^*$  as red as luminous red-sequence galaxies in the cluster core.

Conversely, RXCJ 0014.3-3022 contains a sizeable fraction of actively star-forming systems even within  $R_{200}$  and beyond. This happens in different subregions of this merging cluster for different reasons. sub- $L^*$  starburst systems in the cluster core were discovered by Couch et al. (1998); they experience strong tidal interactions. Both sub- $L^*$  and luminous star-forming systems populate the two filaments stemming out of the cluster main body and reaching  $R_{200}$  and beyond (BPB07). The former can be interpreted as infalling low-mass systems that manage to keep part of their still conspicuous HI gas reservoir, consistently with the generally accepted “downsizing” scenario (Lilly et al. 1996; Gavazzi & Scodeggio 1996; Gavazzi et al. 1996; Cowie et al. 1999), in spite of the growing influence of the cluster environment. The latter were interpreted by BPB07 as relatively high-mass galaxies with residual HI gas in their discs experiencing “harassment” (cf. Moore et al. 1996, 1998, 1999). After an average increase of star-formation activity across  $R_{200}$  (BPB07), star-forming galaxies of all masses along the filaments appear to move towards the red sequence as their cluster-centric distances become smaller and smaller with respect to  $R_{200}$ . This is consistent both with the starvation scenario (Balogh et al. 1999) and with galaxy harassment, as well as with the later removal of residual HI gas through ram pressure stripping by the ICM (e.g., Gunn & Gott 1972; Quilis et al. 2000; Tonnesen & Bryan 2008) in the cluster core.

In conclusion, RXCJ 2308.3-0211 appears as a massive system which is already assembled at  $z \sim 0.3$ , and sits in a large-scale environment where most galaxies are dominated by old, passively evolving stellar populations (cf. the two groups well beyond the cluster virial radius) as well in its virialized region. Conversely, the massive, merging system RXCJ 0014.3-3022 sits in a large-scale environment where galaxies of different masses can still form stars, as it happens in its core and filaments. Nevertheless, galaxies dominated by old, passively evolving stellar populations are the most frequent ones in its core, and define the same locus as those in the core of RXCJ 2308.3-0211, although with half the scatter. This is consistent with the previous picture that a larger and more heterogeneous fraction of the overall galaxy population has stopped forming stars since long or is rapidly moving towards a quiescent star-formation activity in RXCJ 2308.3-0211, whereas in RXCJ 0014.3-3022 only the massive galaxies populating the cluster core have done so.

This is also reflected in the different scatter observed for the two clusters’ red sequences. The tighter red sequence observed in RXCJ 0014.3-3022 can be ascribed to this cluster only having its pristine red sequence, i.e. its primordial population of old, evolved galaxies, the large fraction of observed active objects having not yet moved to the red sequence. Conversely, RXCJ 2308.3-0211 has much less star-forming systems, hence the largest part of the galaxies has already moved to the red sequence. If, consistently with the already described picture, at least part of these galaxies have just recently moved to the red se-

<sup>14</sup> respectively  $1.29$  and  $1.02 \times 10^{45}$  ergs  $s^{-1}$

<sup>15</sup> This is likely even though no correction for dust attenuation is applied to the photometry of star-forming galaxies.

<sup>16</sup> This minimises the impact of dimming and reddening effects produced by dust in star-forming galaxies.

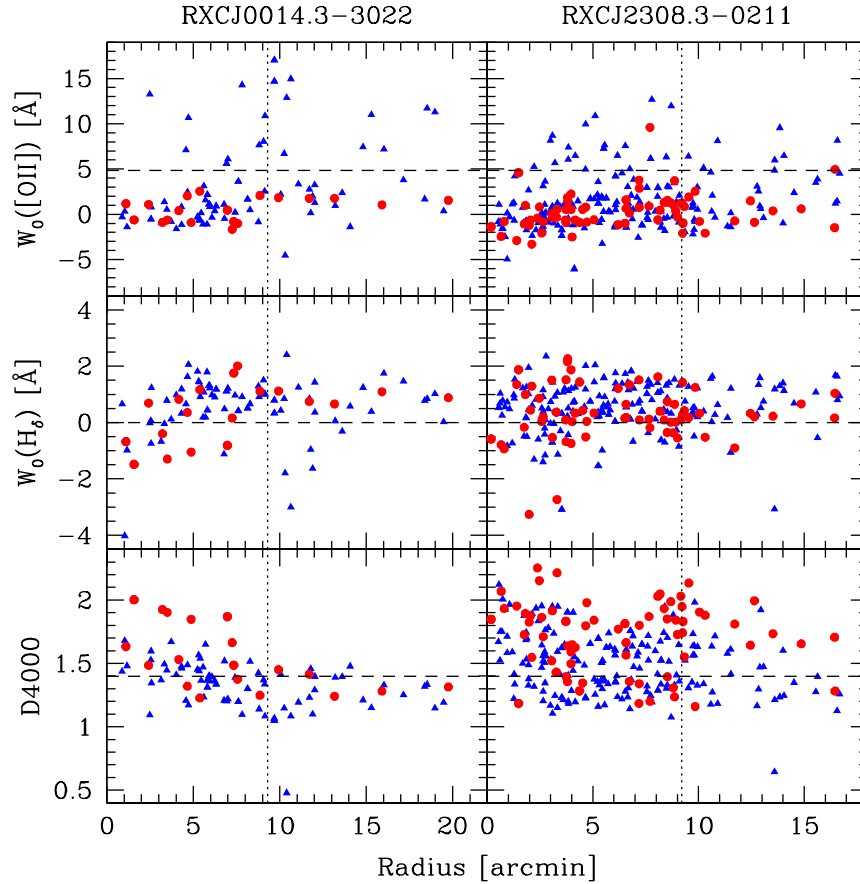


**Fig. 13.** Behaviour of spectral indices as a function of cluster-centric distance for spectroscopic members of RXCJ 0014.3-3022 (left column) and of RXCJ 2308.3-0211 (right column). Symbols are the same as in Fig. 10. In each panel, the horizontal dashed line marks the characteristic threshold for the given index, whereas the vertical dotted line marks the distance corresponding to  $R_{200}$ .

quence, then these younger additions will increase the observed scatter before finally settling on the main red sequence.

Our results support an inside-out scenario for the build-up of the red sequence (e.g. Lidman et al. 2008). They also suggest the existence of a link between assembly history and average star-formation activity in member galaxies of clusters with similar masses in general. This could explain the large variation in the evolutionary phases of galaxies in groups with similar masses since  $z \sim 1$  (Tanaka et al. 2008). Studies based on larger statistics and multiwavelength information than in the present one are necessary to elucidate this matter.

## 5. Conclusions

The link between dynamical state and star-formation history in member galaxies is investigated for two X-ray luminous clusters at  $z \sim 0.3$ , i.e.: the merging system RXCJ 0014.3-3022 and the centrally symmetric system RXCJ 2308.3-0211. The richness of spectroscopic information and the quality of photometric data allow differences in galaxy populations to be traced not only as a function of cluster-centric distance (as done in most previous studies on clusters at similar redshifts), but also of cluster substructure. This is more evident in maps of galaxy overdensity (w.r.t. a coeval, neighbouring “field”) based on the (observed frame) optical colour ( $B - R$ ) and photometric redshifts.

The (observed frame) ( $B - R$ )- $R$  colour-magnitude diagrams of the inner regions of both clusters exhibit the same, well-

defined locus of galaxies dominated by old, passively evolving stellar populations (the so-called red sequence). This locus is more populated, and with a larger scatter around it, in the regular cluster RXCJ 2308.3-0211.

A combined analysis based on spectroscopic indices (i.e., the equivalent widths of the [OII] and  $H_\delta$  lines and the amplitude of the 4000 Å break  $D4000$ ) and (rest frame)  $FUV - V$  colours establishes the existence of substantial differences between the two clusters. In agreement with analogous studies in the literature, the capability of forming stars increases the larger the cluster-centric distance of a member galaxy. There is also evidence for obscured star-formation activity in a small fraction of member galaxies. However, in RXCJ 2308.3-0211, the bulk of the luminous (i.e., with  $L_R \geq L_R^*$ ) galaxy population has stopped forming stars since long, or is evolving towards a quiescent star-formation activity: it’s mostly the sub- $L^*$  galaxies which carry on forming stars at substantial rates. Conversely, RXCJ 0014.3-3022 hosts luminous galaxies with enhanced star-formation activity (w.r.t. the “field”) along two filamentary structures stemming out of its main body and reaching its  $R_{200}$ . Furthermore, an increased fraction of (mostly sub- $L^*$ ) star-forming galaxies is found along the two filaments across  $R_{200}$ . Both phenomena are likely due to “galaxy harassment”. Finally, it was already known that sub- $L^*$  starburst galaxies populate the core of RXCJ 0014.3-3022: they are tidally disturbed systems.

Differences in galaxy populations extend from the virialized regions to the large-scale environments of the two clus-

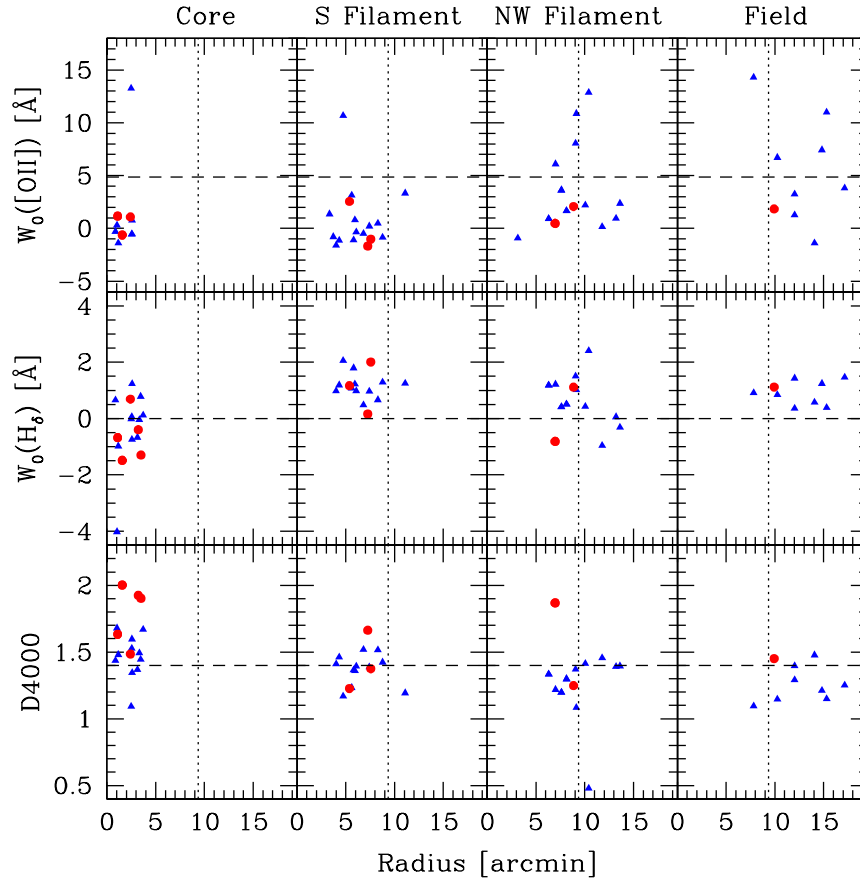


**Fig. 14.** Behaviour of spectral indices as a function of cluster-centric distance for different regions of RXCJ 0014.3-3022 (see Table 5). Symbols and lines are the same as in Fig. 13.

ters. In fact, RXCJ 2308.3-0211 sits in a region of the universe where passive evolution of stellar populations or quiescent star-formation activity characterises at least luminous galaxies, as witnessed by the field and two groups at the same (photometric) redshift. Conversely, the two extended filaments of RXCJ 0014.3-3022 are nested inside a still “active” environment. This suggests the existence of a link between assembly history and average star-formation activity in member galaxies for (at least) X-ray selected, massive clusters at  $z \sim 0.3$ .

**Acknowledgements.** Based on observations made with ESO VLT at the Paranal Observatory under programme ID 169.A-0595. Based on observations made with the ESO/MPG 2.2m telescope at the La Silla Observatory inside the Max Planck Gesellschaft (MPG) time. This research has made use of the NASA/IPAC Extragalactic Database (NED) which is operated by the Jet Propulsion Laboratory, California Institute of Technology, under contract with the National Aeronautics and Space Administration. F.B. acknowledges support by the International Max-Planck Research School (IMPRS) on Astrophysics. D.P. acknowledges support by the German *Deutsches Zentrum für Luft- und Raumfahrt*, DLR project number 50 OR 0405. H.B. acknowledges support by *The Cluster of Excellence “Origin and Structure of the Universe”*, funded by the Excellence Initiative of the Federal Government of Germany, EXC project number 153.

## References

- Abraham, R. G., Smecker-Hane, T. A., Hutchings, J. B., et al. 1996, *ApJ*, 471, 694
- Adami, C., Mazure, A., Biviano, A., Katgert, P., & Rhee, G. 1998a, *A&A*, 331, 493
- Alcalá, J. M., Pannella, M., Puddu, E., et al. 2004, *A&A*, 428, 339
- Arnouts, S., Vandame, B., Benoist, C., et al. 2001, *A&A*, 379, 740
- Baade, D., Meisenheimer, K., Iwert, O., et al. 1999, *Msngr*, 95, 15
- Balogh, M. L., Morris, S. L., Yee, H. K. C., Carlberg, R. G., & Ellingson, E. 1997, *ApJ*, 488, 75
- Balogh, M. L., Morris, S. L., Yee, H. K. C., Carlberg, R. G., & Ellingson, E. 1999, *ApJ*, 527, 54
- Barger, A. J., Aragón-Salamanca, A., Ellis, R. S., et al. 1996, *MNRAS*, 279, 1
- Beers, T. C., Flynn, K., & Gebhardt, K. 1990, *AJ*, 100, 32
- Bertin, E., & Arnouts, S. 1996, *A&A*, 117, 393
- Biviano, A., Girardi, M., Giuricin, G., Mardirossian, F., & Mezzetti, M. 1992, *ApJ*, 396, 35
- Biviano, A., Metcalfe, L., McBreen, B., et al. 2004, *A&A*, 425, 33
- Biviano, A., Murante, G., Borgani, S., et al. 2006, *A&A*, 456, 23
- Böhringer, H., Schuecker, P., Guzzo, L., et al. 2001a, *A&A*, 369, 826
- Böhringer, H., Schuecker, P., Lynam, P., et al. 2001b, *Msngr*, 106, 24
- Böhringer, H., Schuecker, P., Guzzo, L., et al. 2004, *A&A*, 425, 367
- Böhringer, H., Braglia, F., Pierini, D., et al. 2006, *Msngr*, 123, 49
- Böhringer, H., Schuecker, P., Pratt, G. W., et al. 2007, *A&A*, 469, 363
- Bohlin, R. C., Jenkins, E. B., Spitzer, L. Jr., et al. 1983, *ApJS*, 51, 277
- Bolzonella, M., Pelló, R., & Miralles, J. M. 2000, *A&A*, 363, 476
- Boschin, W., Girardi, M., Spolaor, R., & Barrena, R., 2006, *A&A*, 449, 461
- Braglia, F., Pierini, D., & Böhringer, H. 2007, *A&A*, 470, 425 (BPB07)
- Butcher, H., & Oemler, A. Jr., 1978a, *ApJ*, 219, 18
- Butcher, H., & Oemler, A. Jr., 1978b, *ApJ*, 226, 559
- Butcher, H., & Oemler, A. Jr., 1984, *ApJ*, 285, 426
- Coia, D., McBreen, B., Metcalfe, L., Biviano, A., et al. 2005, *A&A*, 431, 433
- Colberg, J. M., White, S. D. M., Jenkins, A., & Pearce, F. R., 1999, *MNRAS*, 308, 593
- Couch, W. J., Barger, A. J., Smail, I., Ellis, R. S., & Sharples, R. M. 1998, *ApJ*, 497, 188
- Cowie, L. L., Songaila, A., & Barger, A. J. 1999, *AJ*, 118, 603
- Dahle, H., Kaiser, N., Irgens, R.J., Lilje, P.B., Maddox, S.J., *ApJS*, 139, 313
- Danese, L., de Zotti, G., & di Tullio, G. 1980, *A&A*, 82, 322
- Davis, M., Huchra, J., Latham, D. W., & Tonry, J. 1982, *ApJ*, 253, 423
- den Hartog, R., & Katgert, P. 1996, *MNRAS*, 279, 349



Dietrich, J. P., Schneider, P., Clowe, D., Romano-Díaz, E., Kerp, J. 2005, *A&A*, 440, 453

Dressler, A. 1980, *ApJ*, 236, 351

Dressler, A., & Gunn, J. E. 1983, *ApJ*, 270, 7

Dressler, A., & Shectman, S. A. 1988, *AJ*, 95, 985

Dressler, A., Oemler, A. Jr., Couch, W. J., et al. 1997, *ApJ*, 490, 577

Dressler, A., Smail, I., Poggianti, B. M., et al. 1999, *ApJS*, 122, 51

Durret, F., Lima Neto, G. B., Forman, W., & Churazov, E. 2003, *A&A*, 403, L29

Ebeling, H., Barrett, E., & Donovan, D. 2004, *ApJ*, 609, L49

Fadda, D., Biviano, A., Marleau, F.R., Storrie-Lombardi, L.J., Durret, F. 2008, *ApJ*, 672, L9

Fasano, Franceschini, 1987, *MNRAS*, 225, 155

Gavazzi, G., & Scodreggio, M. 1996, *A&A*, 312, L29

Gavazzi, G., Pierini, D., & Boselli, A. 1996, *A&A*, 312, 397

Girardi, M., Biviano, A., Giuricin, G., Mardirossian, F., & Mezzetti, M. 1993, *ApJ*, 404, 38

Girardi, M., Giuricin, G., Mardirossian, F., Mezzetti, M., & Boschin, W. 1998, *ApJ*, 505, 74

Gregory, S.A., Thompson, L.A., 1978, *ApJ*, 222, 784.

Gunn, J. E., & Gott, J. R., III 1972, *ApJ*, 176, 1

Halkola, A., Seitz, S., & Pannella, M. 2007, *ApJ*, 656, 739

Horne, K. 1986, *PASP*, 98, 609

Jones, C., & Forman, W. 1992, in *Clusters and superclusters of galaxies*, ed. A. C. Fabian, NATO ASI Series, 366, 49

Katgert, P., Biviano, A., Mazure, A. 2004, *ApJ*, 600, 675

Kempner, J. C., & David, L. 2004, *MNRAS*, 349, 385

Kodama, T., Smail, I., Nakata, F., Okamura, S., Bower, R. G. 2001, *ApJ*, 562, L9

Kodama, T., Smail, I., Nakata, F., Okamura, S., Bower, R. G. 2003, *ApJ*, 591, 169

Kron, R. G. 1980, *ApJS*, 43, 305

Kull, A., & Böhringer, H. 1999, *A&A*, 341, 23

Landolt, A. U. 1992, *AJ*, 104, 340

Le Fèvre, O., Vettolani, G., Garilli, B., et al. 2005, *A&A*, 439, 845

Lidman, C., Rosati, P., Tanaka, M., et al. 2008, *arXiv:0808.2824*

Lilly, S. J., Le Fèvre, O., Hammer, F., Crampton, D. 1996, *ApJ*, 460, L1

Loh, Y., Ellingson, E., Yee, H.K.C., Gilbank, D.G., Gladders, M.D., Barrientos, L.F., 2008, *ApJ*, 680, 214

Metcalfe, L., Fadda, M., Biviano, A., SSRv, 119, 425

McCracken, H. J., Radovich, M., Bertin, E., et al. 2003, *A&A*, 410, 17

Mignano, A., Miralles, J.-M., da Costa, L., et al. 2007, *A&A*, 466, 541

Moore, B., Katz, N., Lake, G., Dressler, A., & Oemler, A. Jr. 1996, *Nature*, 379, 613

Moore, B., Lake, G., & Katz, N. 1998, *ApJ*, 495, 139

Moore, B., Lake, G., Quinn, T., & Stadel, J. 1999, *MNRAS*, 304, 465

Moran, S. M., Ellis, R. S., Treu, T., Smith, G. P., Rich, M., Smail, I. 2007, *ApJ*, 671, 1503

Morris, S. L., Hutchings, J. B., Carlberg, R. G., et al. 1998, *ApJ*, 507, 84

Peacock, 1983, *MNRAS*, 202, 615

Pierini, D., Zibetti, S., Braglia, F., et al. 2008, *A&A*, 483, 727

Poggianti, B. M., Smail, I., Dressler, A., et al. 1999, *ApJ*, 518, 576

Poggianti, B. M., von der Linden, A., De Lucia, G., et al. 2006, *ApJ*, 642, 188

Porter, S.C., Raychaudhury, S., 2007, *MNRAS*, 375, 1409

Porter, S.C., Raychaudhury, S., Pimblett, K.A., Drinkwater, M.J., 2008, preprint, *arXiv:0804.4177*

Quilis, V., Moore, B., & Bower, R. 2000, *Science*, 288, 1617

Renzini, A., & da Costa, L. 1997, *Msngr*, 87, 23

Robin, A. C., Reylé, C., Derrière, S., & Picaud, S. 2003, *A&A*, 409, 523

Saintonge, A., Tran, K.V.H., Holden, B.P. 2008, *arXiv:0806.2157*

Scharf, C., Donahue, M., Voit, G. M., Rosati, P., & Postman, M. 2000, *ApJ*, 528, L73

Schechter, P. 1976, *ApJ*, 203, 297

Schlegel, D. J., Finkbeiner, D. P., & Davis, M. 1998, *ApJ*, 500, 525

Scodreggio, M., Franzetti, P., Garilli, B., et al. 2005, *PASP*, 117, 1284

Selman, F. J. 2004, in *Optimizing Scientific Return for Astronomy through Information Technologies*, ed. P. J. Quinn, & A. Bridger (SPIE 5493) 453

Tanaka, M., Finoguenov, A., Kodama, T., et al. 2008, *arXiv:0808.1961*

Tonnesen, S., & Bryan, G. L. 2008, *arXiv:0808.0007*

Tran, K.-V. H., van Dokkum, P., Illingworth, G. D., Kelson, D., Gonzalez, A., Franx, M., 2005, *ApJ*, 619, 134

Vandame, B. 2004, PhD thesis, University of Nice-Sophia Antinopolis

Verdugo, M., Ziegler, B. L., & Gerken, B. 2008 *A&A*, 486, 9

Whitmore, B.C., Gilmore, D., & Jones, C. 1993, *ApJ*, 407, 489

Wilman, D. J., et al. 2008, *ApJ*, 680, 1009

Zappacosta, L., Mannucci, F., Maiolino, R., et al., 2002, *A&A*, 394, 7

Zhang, Y.-Y., Böhringer, H., Finoguenov, A., et al. 2006, *A&A*, 456, 55

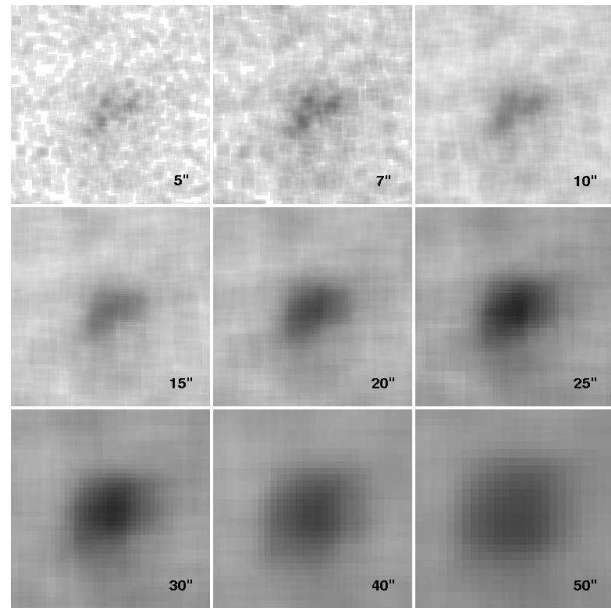


**Fig. A.1.** Example of density map for the central part of A2744. From top left to bottom right, density maps for different mesh widths are shown. The mesh width value in arcseconds is also shown for each map.

## Appendix A: Density map calculation

Starting from the main catalogue of cluster photo-*z* members and the two sub-catalogues of red and blue objects, a fixed-width mesh is applied to the full catalogue. The mesh width is found to partly affect the final density map, mainly by smoothing small-scale density peaks; its best value is found to be between 7 and 10 arcsec, corresponding to a physical scale of 30 to 45 kpc at the cluster's redshift. To ensure a better sampling of the cluster population, a scale of 10 arcseconds was chosen. This is a small enough scale to detect and suitably map substructures in dense regions (like the cluster core where three main prominent blobs are seen in the galaxy distribution), while ensuring a good and stable sampling of low-density regions without being heavily affected by small-scale background fluctuations. A fixed mesh width is found to better map both high-density peaks and background, while adaptive meshes proved to be too sensitive to small-scale fluctuations, with the risk of a wrong evaluation of background.

Background is calculated in each mesh point by counting all objects in a fixed radius around the point. The chosen radius partly acts as a smoothing filter: this ensures a good sampling of the large-scale shape of background (so to be able to correctly evaluate background mean and RMS). The background mean value and RMS are then calculated by fitting the background values distribution with a gaussian, assuming that the field should represent a population of randomly scattered objects with normal fluctuations. The gaussian is fitted through recursive 3-sigma clipping until convergence, which is always reached with 3 to 10 cycles. The final gaussian parameters are taken as mean and RMS of background.

To select the most efficient smoothing radius, several test were run on the sample with different radius values. The background was thus calculated with increasing radii and then fitted with a gaussian, assuming it is dominated by random noise (i.e. randomly scattered field galaxies). The background mean value and RMS are weakly sensitive to the smoothing radius for radius

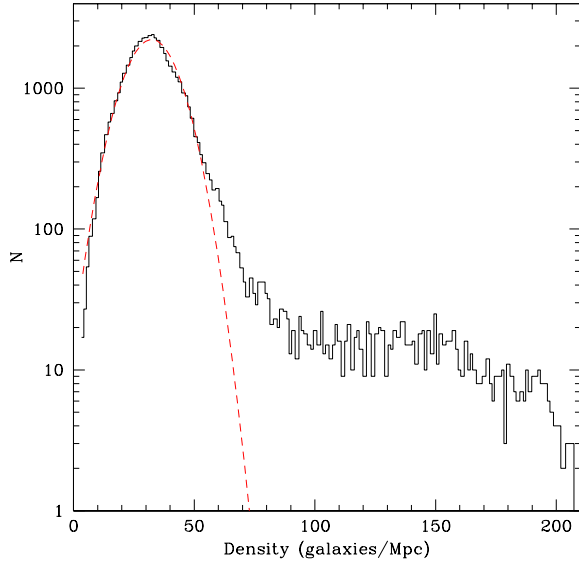


**Fig. A.2.** Background fit for a smoothing radius of  $110''$  in the field of RXCJ0014.3-3022. The histogram is the count distribution in the field, with the high density tail due to overdense structures (i.e. the cluster and its filaments); the dashed line is the gaussian fit to the background.

values between  $60''$  and  $120''$ . Below  $60''$ , small-scale fluctuations make the background dominated by small numbers, while beyond  $120''$  the mean goes slowly but steadily down, due to undersampling of background counts at the field borders. Between  $60''$  and  $120''$  the background value is almost stable, with errors becoming slightly lower with increasing smoothing radius. The behaviour, along with the background RMS, is shown in Fig. A.3. A final smoothing scale of  $110''$  was chosen; this is equivalent to  $500$  kpc at the cluster redshift.

After evaluating background mean and RMS, the true density maps are generated. First, galaxies are counted in each mesh box and their number is divided by the box area and then normalised to Mpc scale. The map is then smoothed with a gaussian filter to clean numerical spikes (arising at the map border due to wrong sampling) and for better, continuous connection of counts in neighboring mesh cells. The same smoothing radius as for background calculation gives reliable results, cleaning spikes without deleting substructuring information. A number of simulated background maps is then generated as randomly distributed values with normal distribution (as given by the background best-fit parameters and chosen smoothing scale); the background map is then independently subtracted from the raw density map and the resulting background-subtracted maps are stacked together and normalised. This ensures a background subtraction as smooth as possible and unaffected by true overdensities in the cluster field. 100 iterations already give a good mean background subtraction.

The background-subtracted, stacked and normalised image is in the end taken as the final surface density map of the field.

## Appendix B: Spectroscopic catalogue of RXCJ0014.3-3022 (A2744)

Hereafter the full catalogue of spectroscopic objects in the field of RXCJ0014.3-3022 is provided. Along with position and redshift, for each object are also provided the values of spectral in-

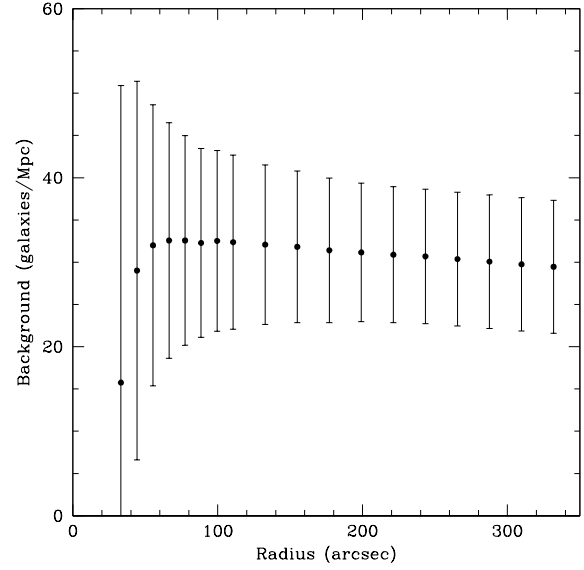


**Fig. A.3.** Background mean and error versus smoothing radius for the full catalogue of cluster members. For very low values (under  $60''$ ) the value rapidly goes down due to oversampling of small fluctuations, while beyond  $120''$  a trend towards lower values is due to undersampling of counts at the field border. Between  $60''$  and  $120''$ , the background value is stable. Error bars are  $1\sigma$  errors.

indices and BVR magnitudes with corresponding errors. Where equivalent widths were not calculated due to the line not being sampled in the instrument's spectral range, the table reads ND, i.e. Not Detected.

## Appendix C: Spectroscopic catalogue of RXCJ2308.3-0211 (A2537)

Hereafter the full catalogue of spectroscopic objects in the field of RXCJ2308.3-0211 is provided. Along with position and redshift, for each object are also provided the values of spectral indices and BVR magnitudes with corresponding errors. Where equivalent widths were not calculated due to the line not being sampled in the instrument's spectral range, the table reads ND, i.e. Not Detected.